# Sensor-Based Reactive Navigation in Unknown Convex Sphere Worlds

The International Journal of Robotics Research
XX(X):1–28

DOI: 10.1177/ToBeAssigned
www.sagepub.com/
SAGE

**Omur Arslan and Daniel E. Koditschek**

**Abstract**

We construct a sensor-based feedback law that provably solves the real-time collision-free robot navigation problem in a compact convex Euclidean subset cluttered with unknown but sufficiently separated and strongly convex obstacles. Our algorithm introduces a novel use of separating hyperplanes for identifying the robot's local obstacle-free convex neighborhood, affording a reactive (online-computed) continuous and piecewise smooth closed-loop vector field whose smooth flow brings almost all configurations in the robot's free space to a designated goal location, with the guarantee of no collisions along the way. Specialized attention to planar navigable environments yields a necessary and sufficient condition on convex obstacles for almost global navigation towards any goal location in the environment. We further extend these provable properties of the planar setting to practically motivated limited range, isotropic and anisotropic sensing models, and the nonholonomically constrained kinematics of the standard differential drive vehicle. We conclude with numerical and experimental evidence demonstrating the effectiveness of the proposed sensory feedback motion planner.

**Keywords**

Robot motion planning and control, feedback motion planning, sensor-based motion planning, artificial potential fields, navigation functions, collision avoidance, local free space, separating hyperplanes, Voronoi diagrams

## 1 Introduction

Agile navigation in dense human crowds Trautman et al. (2015); Henry et al. (2010), or in natural forests, such as now negotiated by rapid flying Karaman and Frazzoli (2012); Paranjape et al. (2015) and legged Wooden et al. (2010); Johnson et al. (2011) robots, strongly motivates the development of sensor-based reactive motion planners, even for the relatively simple environmental models (disk punctured planes) that seem to describe them Ilhan et al. (2018). By the term *reactive* Choset et al. (2005); LaValle (2006) we mean that motion is generated by a vector field arising from some closed-loop feedback policy issuing online force or velocity commands in real time as a function of instantaneous robot state. By the term *sensor-based* we mean that information about the location of the environmental clutter to be avoided is limited to structure perceived within some local neighborhood of the robot's instantaneous position — its sensor footprint.

In this paper, we propose a new reactive motion planner taking the form of a feedback law for a first-order (velocity-controlled), perfectly sensed and actuated disk-shaped robot, relative to a fixed goal location, that can be computed using only information about the robot's instantaneous position and structure within its sensor footprint. We assume the a priori unknown environment is a static topological sphere world Koditschek and Rimon (1990), whose obstacles are convex and have smooth boundaries whose curvature is "reasonably" high relative to their mutual separation; and we identify the intrinsic geometric structure within the robot's sensory footprint using separating hyperplanes between the robot body and sensed (convex) obstacles Boyd and Vandenberghe (2004). Under these assumptions, the proposed closed-loop vector field is guaranteed to bring almost[1] all (i.e., excluding at most a measure zero subset of) initial conditions to the desired goal. To the best of our knowledge, this is the first time a sensor-based reactive motion planner has been shown to be provably correct with respect to a general class of environments.

Department of Electrical and Systems Engineering, University of Pennsylvania, USA

**Corresponding author:**
Omur Arslan, Department of Electrical and Systems Engineering, University of Pennsylvania, Philadelphia, PA 19104, USA.
Email: omur@seas.upenn.edu

## 1.1 Motivation and Related Work

*1.1.1 Feedback Motion Planning:* The simple, computationally efficient artificial potential field[2] approach to real-time obstacle avoidance Khatib (1986) incurs topologically necessary critical points Koditschek (1987b), which, in practice, with no further remediation often include (topologically unnecessary) spurious local minima. In general, such local obstacle avoidance strategies Borenstein and Koren (1991); Simmons (1996); Fox et al. (1997); Fiorini and Shiller (1998) yield safe robot navigation algorithms but offer no assurance of (global) convergence to a designated goal location. Even in topologically simple settings such as the sphere worlds addressed here, constructions that eliminate these spurious attractors — e.g., navigation functions Rimon and Koditschek (1992), or other methods Connolly and Grupen (1993) — have largely come at the price of complete prior information. Although, harmonic functions can be utilized to design potential functions without local minima Connolly and Grupen (1993), such intrinsically numerical constructions forfeit the reactive nature of feedback motion planners under discussion here. Hence, navigation functions (Koditschek and Rimon 1990), when they can be explicitly constructed, for example, as in Rimon and Koditschek (1992) offer the only available gradient-based reactive navigation approach in the literature that provably resolves the local minima problem of more general artificial potential functions Khatib (1986). Analyzing directly the properties of the Rimon-Koditschek navigation function within the class of convex sphere worlds similar to that addressed here Paternain et al. (2017), yields a stochastic extension with provable convergence properties Paternain and Ribeiro (2016) that may in practice permit its implementation in settings where only local, noisy sensor information is available.

Extensions to the navigation function framework partially overcoming the necessity of global prior knowledge of (and consequent parameter tuning for) a topologically and metrically simple environment have appeared in the last decade Lionis et al. (2007); Filippidis and Kyriakopoulos (2011). Adjustable navigation functions are proposed to gradually update the tuning parameter upon the discovery of new obstacles Filippidis and Kyriakopoulos (2011), and locally computable navigation functions are introduced by restricting the effect of each obstacle in its immediate vicinity such that a robot is required to deal with at most one obstacle at a time Lionis et al. (2007) Ilhan et al. (2018). Moreover, sequential composition Burridge et al. (1999) has been used to cover metrically complicated environments with convex cell-based local potential decompositions Conner et al. (2009) (and extended to nonholonomically constrained finite size robots Conner et al. (2011)), but still requires prior global knowledge of the environment.

*1.1.2 Spatial Decomposition in Motion Planning:* Spatial decomposition methods are commonly encountered in motion planning for modeling the connectivity of configuration spaces and for increasing the computational performance of motion planners by substantially reducing the associated search space Choset et al. (2005); LaValle (2006). For example, generalized Voronoi diagrams Ó'Dúnlaing and Yap (1985); Choset and Burdick (2000) and cell decomposition methods Chazelle (1987); Choset and Pignon (1998) are typically used in the design of roadmap methods LaValle (2006); Ó'Dúnlaing and Yap (1985); Choset and Burdick (2000) that construct a global, one-dimensional graphical representation (skeleton) of a configuration space (independent of any specific robot configuration) and seek for a connected path in this skeleton to navigate a robot between any source-destination pair. A major distinction of our construction from these roadmap algorithms is that we follow a local, online, robot-centric spatial decomposition approach to determine a safe neighborhood of a robot configuration that also captures the local geometric structure of the configuration space around the robot's instantaneous position. In a broader perspective, we view our approach as an application of clustering, an unsupervised learning method, for automatically extracting intrinsic structures in configuration spaces Arslan et al. (2016); Arslan (2016).

Typically, in sampling-based motion planning, retraction onto the medial axis of a configuration space Wilmarth et al. (1999); Holleman and Kavraki (2000) and cell decomposition methods Foskey et al. (2001); van den Berg and Overmars (2005) are heuristically applied to bias sampling along the skeleton of the configuration space, especially, in order to efficiently find a path around narrow passages. In our numerical and experimental studies, summarized in Section 6 and Section 7, respectively, we also observe a similar desired motion pattern: our vector field motion planner balances the robot's distance to nearby obstacles while safely steering the robot towards its destination location. Thus, we believe that the proposed approach offers a novel unifying framework that simultaneously integrates desired features of feedback motion planning and roadmap methods. For example, in recent papers Arslan et al. (2017); Pacelli et al. (2018), we have shown how the proposed navigation method in this paper can be adapted to build a sensory steering algorithm for sampling-based motion planning in complex environments with narrow passages. Or, again, in Vasilopoulos et al. (2018) we use extensions Arslan and Koditschek (2017) of the ideas presented here to develop a mobile manipulation scheme that merges an offline deliberative task planner with a variant of our reactive motion planner with provable guarantees of safe, correct completion.

Finally, it is worth noting that our use of robot-centric spatial decomposition is motivated by the application of Voronoi diagrams in robotics for coverage control of distributed mobile sensor networks Cortés et al. (2004); Kwok and Martnez (2010); Pimenta et al. (2008); Arslan and Koditschek (2016c), where robot-centric Voronoi decomposition solves the sensory task assignment problem in mobile sensor networks. Beyond their use in optimal sensor allocation problems, we introduced in Arslan and Koditschek (2016c) the application of robot-centric Voronoi diagrams to the problem of multirobot collisions. Subsequently, similar uses of Voronoi diagrams for collision avoidance have received attention in the multirobot navigation Zhou et al. (2017) and cluttered tracking Pierson and Rus (2017) literature as well as for autonomous lane change Wang et al. (2018). In none of these settings (navigation, tracking, or lane change, respectively) it was shown that the task could be achieved without the possibility of entering a deadlock situation. Thus, to the best of our knowledge, this is the first work to present sufficient (and, for the 2D case, necessary) conditions on an environment that guarantee a greedy reactive navigation strategy can achieve global single robot navigation while ensuring safety.

## 1.2 Summary of Contributions

This paper abandons the smooth potential field approach to reactive planning, achieving an algorithm that is "doubly reactive" in the sense that not merely the integrated robot trajectory, but also its generating vector field can be constructed on the fly in real time using only local knowledge of the environment. Our piecewise smooth vector field combines some of the ideas of sensor-based exploration Choset and Burdick (2000) with those of hybrid reactive control Conner et al. (2009). We use separating hyperplanes of convex bodies Boyd and Vandenberghe (2004) to identify an obstacle-free convex neighborhood of a robot configuration, and build our safe robot navigation field by control action towards the metric projection Webster (1995) of the designated point destination onto this convex set.

Our construction, guaranteed to converge with no collisions in spaces of arbitrary (finite) dimension, requires no parameter tuning and requires only local knowledge of the environment in the sense that the robot need only locate those proximal obstacles determining its collision-free convex neighborhood. When the obstacles are sufficiently separated (Assumption 1 stipulates that the robot must be able to pass in between them) and sufficiently strongly convex at their "antipode" (Assumption 2 stipulates that they curve away from the enclosing sphere centered at the destination which just touches their boundary at the most distant point), the proposed vector field generates a smooth flow with a unique attractor at the specified goal location along with (the topologically necessary number of) saddles — at least one associated with each obstacle. Since all of its critical points are nondegenerate, our vector field is guaranteed to steer almost[1] all collision-free robot configurations to the goal, while avoiding collisions along the way, as illustrated in Fig. 1.

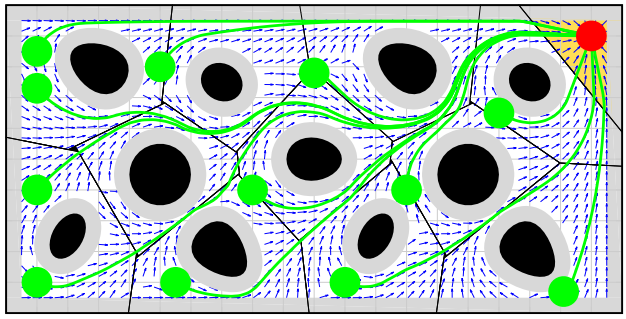

**Fig. 1.** Exact navigation of a disk-shaped robot using separating hyperplanes of the robot body (red at the goal) and convex obstacles (black solid shapes). Separating hyperplanes between the robot and obstacles define an obstacle-free convex neighborhood (the yellow region when the robot at the goal) of the robot, and the continuous feedback motion towards the metric projection of a given desired goal (red) onto this convex set asymptotically steers almost[1] all robot configurations (green) to the goal with no collisions (from any initial condition) along the way. The grey regions represent the augmented workspace boundary and obstacles, and the arrows depict the direction of the resulting vector field.

It proves most convenient to develop the theoretical properties of this construction under the assumption that the robot can identify and locate those nearby obstacles whose associated separating hyperplanes define its obstacle-free convex neighborhood (a capability termed *Voronoi-adjacent obstacle sensing* in Section 3.2). Then, to accommodate more physically realistic sensors, we adapt the initial construction (and the proof) to the case of two different limited range sensing modalities. Next, in the interest of greater practicability, we further extend the construction (and the proof) to the case of the commonly encountered kinematic differential drive vehicle model (retaining the convergence and collision avoidance guarantees, at the necessary cost of a discontinuous feedback law), with isotropic and anisotropic sensory capabilities. Finally, we demonstrate the effectiveness of these various navigation algorithms by reporting the results of numerous numerical simulations and experimental studies with a physical robot.

In a prior conference paper Arslan and Koditschek (2016a), we proposed a different construction based on power diagrams Aurenhammer (1987) for navigating

among spherical obstacles using knowledge of Voronoi-adjacent[3] obstacles to construct the robot's local workspace (Arslan and Koditschek 2016a, Eqn. (9)). In a subsequent conference paper Arslan and Koditschek (2016b), we introduced a new construction for that set in (8) based on separating hyperplanes, permitting an extension of the navigable obstacles to the broader class of convex bodies specified by Assumption 2, while providing the same guarantee of almost[1] global asymptotic convergence (Theorem 3) to a given goal location. From the view of applications, the new appeal to separating hyperplanes permits the central advance of a purely reactive construction from limited range sensors (24) — e.g., in the planar case from immediate line-of-sight appearance (30) — with the same global guarantees. This paper gives a unified view of these results (with some tutorial background and detailed discussions) and provides experimental validation of the results.

### 1.3 Organization of the Paper

The rest of this paper is organized as follows. Section 2 continues with a formal statement of the problem at hand. Section 3 briefly summarizes a separating hyperplane theorem for convex bodies, and introduces its use for identifying collision-free robot configurations. Section 4 constructs and analyzes the reactive vector field planner for safe robot navigation in a convex sphere world, and provides its more practical extensions for various sensing modalities and actuation models. Section 5 presents a brief discussion of planar navigable environments for greedy navigation strategies, such as the one constructed in this paper. Section 6 and Section 7 illustrate the qualitative properties of the proposed vector field planner using numerical simulations and experimental results, respectively. Section 8 concludes with a summary of our contributions and a brief discussion of future work.

## 2 Problem Formulation

Consider a disk-shaped robot, of positive radius $r \in \mathbb{R}_{>0}$ centered at $\mathrm{x} \in \mathcal{W}$, operating in a closed compact convex environment $\mathcal{W}$ in the $n$-dimensional Euclidean space $\mathbb{R}^n$, where $n \geq 2$, punctured by $m \in \mathbb{N}$ open convex sets $\mathcal{O} := \{O_1, O_2, \ldots, O_m\}$ with twice differentiable boundaries, representing obstacles.[4] Hence, the free space $\mathcal{F}$ of the robot is given by

$$\mathcal{F} := \left\{ \mathrm{x} \in \mathcal{W} \,\middle|\, \overline{B(\mathrm{x}, r)} \subseteq \mathcal{W} \setminus \bigcup_{i=1}^{m} O_i \right\}. \tag{1}$$

where $B(\mathrm{x}, r) := \left\{ \mathrm{q} \in \mathbb{R}^n \middle| \|\mathrm{q} - \mathrm{x}\| < r \right\}$ is the open ball centered at x with radius $r$, $\overline{B(\mathrm{x}, r)}$ denotes its closure, and $\|.\|$ denotes the standard Euclidean norm.

To maintain the local convexity of obstacle boundaries in the free space $\mathcal{F}$, we assume that our disk-shaped robot can freely fit in between (and thus freely circumnavigate) any of the obstacles throughout the workspace $\mathcal{W}$, which is generally refered to as the "isolated" obstacles assumption Rimon and Koditschek (1992):

**Assumption 1.** *Obstacles are separated from each other by clearance of at least*

$$d(O_i, O_j) > 2r, \quad \forall i \neq j, \tag{2}$$

*and from the boundary $\partial\mathcal{W}$ of the workspace $\mathcal{W}$ as*

$$d(O_i, \partial\mathcal{W}) > 2r, \quad \forall i, \tag{3}$$

*where $d(A, B) := \inf\left\{ \|\mathrm{a} - \mathrm{b}\| \,\middle|\, \mathrm{a} \in A, \mathrm{b} \in B \right\}$.*

Before formally stating our navigation problem, it is useful to recall a specific consequence of the well known topological limitation of reactive planners: if a continuous vector field planner on a generalized sphere world has a unique attractor, then it must have at least as many saddles as obstacles Koditschek and Rimon (1990). In consequence, the robot navigation problem that we seek to solve is stated as:

**Reactive Navigation Problem** *Assuming the first-order (fully-actuated single-integrator) robot dynamics,*

$$\dot{\mathrm{x}} = \mathrm{u}(\mathrm{x}), \tag{4}$$

*find a Lipschitz continuous controller, $\mathrm{u} : \mathcal{F} \to \mathbb{R}^n$, that leaves the robot's free space $\mathcal{F}$ positively invariant and asymptotically steers almost[1] all configurations in $\mathcal{F}$ to any given goal $\mathrm{x}^* \in \mathcal{F}$.*

## 3 Encoding Collisions via Separating Hyperplanes

In this section, we briefly recall a separating hyperplane theorem for disjoint convex sets, and then adapt it to identify a collision-free neighborhood of a disk-shaped robot.

### 3.1 Separating Hyperplane Theorem

A fundamental result of convexity theory states that any two disjoint convex sets can be separated by a hyperplane such that they lie on opposite sides of this hyperplane:

**Theorem 1.** Separating Hyperplane Theorem Webster (1995); Boyd and Vandenberghe (2004). *For any two nonintersecting convex sets $A, B \in \mathbb{R}^n$ (i.e., $A \cap B = \varnothing$), there exists $\mathrm{a} \in \mathbb{R}^n$ and $b \in \mathbb{R}$ such that $\mathrm{a}^{\mathrm{T}}\mathrm{x} \geq b$ for all $\mathrm{x} \in A$ and $\mathrm{a}^{\mathrm{T}}\mathrm{x} \leq b$ for all $\mathrm{x} \in B$.*

For example, a usual choice of such a hyperplane is Boyd and Vandenberghe (2004):

**Definition 1** The *maximum margin separating hyperplane* of any two disjoint convex sets $A, B \subset \mathbb{R}^n$, with $d(A,B) > 0$, is defined to be

$$H(A,B) := \left\{ \mathrm{x} \in \mathbb{R}^n \,\middle|\, \|\mathrm{x}-\mathrm{a}^*\| = \|\mathrm{x}-\mathrm{b}^*\|, (\mathrm{a}^*,\mathrm{b}^*) = \underset{\mathrm{a}\in\overline{A},\mathrm{b}\in\overline{B}}{\arg\min}\, d(\mathrm{a},\mathrm{b}) \right\},$$

where $d(\mathrm{x}, H(A,B)) \geq \frac{d(A,B)}{2}$ for all $\mathrm{x} \in A \cup B$.

It is useful to remark that although there can be more than one pair of points $\mathrm{a} \in \overline{A}$ and $\mathrm{b} \in \overline{B}$ achieving $\|\mathrm{a}-\mathrm{b}\| = d(A,B)$, they all define the same maximum margin separating hyperplane (Lemma 4).

Another useful tool for finding a separating hyperplane between a point and a convex set is metric projection:

**Theorem 2.** Webster (1995). *Let $A \subset \mathbb{R}^n$ be a closed convex set and $\mathrm{x} \in \mathbb{R}^n$. Then there exists a unique point $\mathrm{a}^* \in A$ such that*

$$\mathrm{a}^* = \Pi_A(\mathrm{x}) := \underset{\mathrm{a}\in A}{\arg\min} \|\mathrm{a}-\mathrm{x}\|, \tag{5}$$

*and one has $(\mathrm{x}-\Pi_A(\mathrm{x}))^{\mathrm{T}}(\Pi_A(\mathrm{x})-\mathrm{a}) \geq 0$ for all $\mathrm{a} \in A$.*

*The map $\Pi_A(\mathrm{x})$ is called the* metric projection *of $\mathrm{x}$ onto set $A$.*

Hence, it is straightforward to observe that:

**Lemma 1.** *The maximum margin separating hyperplane of a convex set $A \subset \mathbb{R}^n$ and the ball $B(\mathrm{x},r)$ of radius $r \in \mathbb{R}_{>0}$ centered at $\mathrm{x} \in \mathbb{R}^n$, satisfying $d(\mathrm{x},A) \geq r$, is given by*

$$H(A,B(\mathrm{x},r)) = \left\{ \mathrm{y} \in \mathbb{R}^n \,\middle|\, \left\| \mathrm{y} - (\Pi_{\overline{B(\mathrm{x},r)}} \circ \Pi_{\overline{A}})(\mathrm{y}) \right\| = \|\mathrm{y} - \Pi_{\overline{A}}(\mathrm{x})\| \right\}, \tag{6}$$

*where* $(\Pi_{\overline{B(\mathrm{x},r)}} \circ \Pi_{\overline{A}})(\mathrm{x}) = \mathrm{x} - r\frac{\mathrm{x}-\Pi_{\overline{A}}(\mathrm{x})}{\|\mathrm{x}-\Pi_{\overline{A}}(\mathrm{x})\|}$.

**Proof.** See Appendix B.1. ■

A common application of separating hyperplanes of a set of convex bodies is to discover their organizational structure. For instance, to model its topological structure, we define the generalized Voronoi diagrams $\mathcal{V} = \{V_1, V_2, \ldots, V_m\}$ of a convex environment $\mathcal{W}$ in $\mathbb{R}^n$ populated with disjoint convex obstacles $\mathcal{O} = \{O_1, O_2, \ldots, O_m\}$ (i.e., $d(O_i, O_j) > 0 \ \forall i \neq j$), based on maximum margin separating hyperplanes, to be

$$V_i := \left\{ \mathrm{q} \in \mathcal{W} \,\middle|\, \|\mathrm{q}-\mathrm{p}_i^*\| \leq \|\mathrm{q}-\mathrm{p}_j^*\|, \ (\mathrm{p}_i^*, \mathrm{p}_j^*) = \underset{\mathrm{p}_i\in\overline{O}_i, \mathrm{p}_j\in\overline{O}_j}{\arg\min}\, d(\mathrm{p}_i,\mathrm{p}_j) \ \ \forall j \neq i \right\}, \tag{7}$$

which yields a convex cell decomposition of a subset of $\mathcal{W}$ such that, by construction, each obstacle is contained in its Voronoi cell, i.e., $O_i \subset V_i$, see Fig. 2. Note that for point obstacles, say $O_i = \{\mathrm{p}_i\}$ for some $\mathrm{p}_i \in \mathbb{R}^n$, the generalized Voronoi diagram of $\mathcal{W}$ in (7) simplifies back to the standard Voronoi diagram of $\mathcal{W}$, generated by points $\{\mathrm{p}_1, \ldots, \mathrm{p}_m\}$, i.e., $V_i = \left\{ \mathrm{q} \in \mathcal{W} \,\middle|\, \|\mathrm{q}-\mathrm{p}_i\| \leq \|\mathrm{q}-\mathrm{p}_j\|, \forall j \neq i \right\}$ Okabe et al. (2000).

## 3.2 Safe Neighborhood of a Robot

Throughout the sequel, we consider a disk-shaped robot, centered at $\mathrm{x} \in \mathcal{W}$ with radius $r \in \mathbb{R}_{>0}$, moving in a closed compact convex environment $\mathcal{W} \subseteq \mathbb{R}^n$ populated with open convex obstacles, $\mathcal{O} = \{O_1, O_2, \ldots, O_m\}$, satisfying Assumption 1. Since the workspace, obstacles, and the robot radius are fixed, we suppress all mention of the associated terms wherever convenient, in order to simplify the notation.

Using the robot body and obstacles as generators of a generalized Voronoi diagram of $\mathcal{W}$, we define the robot's *local workspace*, $\mathcal{LW}(\mathrm{x})$, illustrated in Fig. 2(left), as,

$$\mathcal{LW}(\mathrm{x}) := \left\{ \mathrm{q} \in \mathcal{W} \,\middle|\, \left\| \mathrm{q} - \mathrm{x} + r\frac{\mathrm{x}-\Pi_{\overline{O}_i}(\mathrm{x})}{\|\mathrm{x}-\Pi_{\overline{O}_i}(\mathrm{x})\|} \right\| \leq \|\mathrm{q}-\Pi_{\overline{O}_i}(\mathrm{x})\|, \forall i \right\}, \tag{8}$$

where, to solve the indeterminacy, we set $\frac{\mathrm{y}}{\|\mathrm{y}\|} = 0$ whenever $\mathrm{y} = 0$. Note that we here take the advantage of having a disk-shaped robot and construct the maximum margin separating hyperplane between the robot and each obstacle using the robot's centroid (Lemma 1), which will become more significant in the sequel for a fixed radius sensory footprint and a limited range line-of-sight sensor.

A critical property of the local workspace $\mathcal{LW}$ is:

**Proposition 1.** *A robot placement $\mathrm{x} \in \mathcal{W} \setminus \bigcup_{i=1}^m O_i$ is collision free, i.e., $\mathrm{x} \in \mathcal{F}$, if and only if the robot body is contained in its local workspace $\mathcal{LW}(\mathrm{x})$, i.e.,*[5] [6]

$$\mathrm{x} \in \mathcal{F} \iff \overline{B(\mathrm{x},r)} \subseteq \mathcal{LW}(\mathrm{x}). \tag{9}$$

**Proof.** See Appendix B.2. ■

Accordingly, we define the robot's *local free space*, $\mathcal{LF}(\mathrm{x})$, by eroding $\mathcal{LW}(\mathrm{x})$, removing the volume swept along its boundary, $\partial\mathcal{LW}(\mathrm{x})$, by the robot body radius Haralick et al. (1987), illustrated on the left in Fig. 2, as

$$\mathcal{LF}(\mathrm{x}) := \mathcal{LW}(\mathrm{x}) \setminus \big(\partial\mathcal{LW}(\mathrm{x}) \oplus B(\mathbf{0},r)\big), \tag{10a}$$

$$= \left\{ \mathrm{q} \in \mathcal{LW}(\mathrm{x}) \,\middle|\, \overline{B(\mathrm{q},r)} \subseteq \mathcal{LW}(\mathrm{x}) \right\}. \tag{10b}$$

where $\mathbf{0}$ is a vector of all zeros with the appropriate size, and $A \oplus B$ denotes the Minkowski sum of sets $A$ and $B$, defined as $A \oplus B = \{a+b \mid a \in A, b \in B\}$. Note that, for any $\mathrm{x} \in \mathcal{F}$, $\mathcal{LF}(\mathrm{x})$ is a nonempty closed convex set, because $\mathrm{x} \in \mathcal{LF}(\mathrm{x})$ and the erosion of a closed convex set by an open ball is a closed convex set.[7]

An immediate consequence of Proposition 1 is:

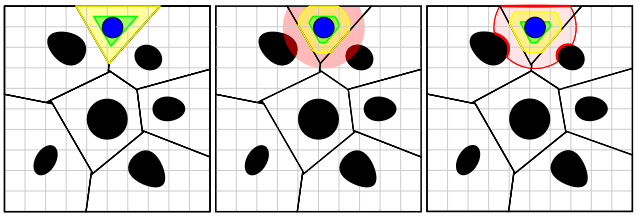

**Fig. 2.** Local workspace $\mathcal{LW}$ (yellow) and local free space $\mathcal{LF}$ (green) of a disk-shaped robot (blue) for different sensing modalities: (left) Voronoi-adjacent[3] obstacle sensing, (middle) a fixed radius sensory footprint (red), (right) a limited range line-of-sight sensor (red). The boundary of each generalized Voronoi cell is defined by the maximum margin separating hyperplanes of the robot body (blue) and obstacles (black).

**Corollary 1.** *Any robot placement in the local free space $\mathcal{LF}(\mathrm{x})$ of a collision-free robot location $\mathrm{x} \in \mathcal{F}$ is also collision free, i.e., $\mathcal{LF}(\mathrm{x}) \subseteq \mathcal{F}$ for all $\mathrm{x} \in \mathcal{F}$.*

Finally, it is worth observing that to construct its local workspace, the robot requires only local knowledge of the environment in the sense that it need merely locate proximal obstacles — those whose Voronoi cells are adjacent[3] to it (i.e., to its local workspace). This can be achieved by assuming an adjustable radius sensory footprint and gradually increasing its sensing range until the set of obstacles in the sensing range satisfies a certain geometric criterion guaranteeing that the detected obstacles exactly define the robot's local workspace Cortés et al. (2004). We will refer to this sensing model as *Voronoi-adjacent obstacle sensing*.

## 4 Exact Robot Navigation via Separating Hyperplanes

In this section, first assuming Voronoi-adjacent obstacle sensing, we introduce a new provably correct vector field controller for safe robot navigation in a convex sphere world, and list its important qualitative properties. Then we present its extensions for two more realistic sensor models (illustrated, respectively, in the middle and the right panels of Fig. 2): a fixed radius sensory footprint and a limited range line-of-sight sensor. We further adapt our construction to the widely used nonholonomically constrained differential drive vehicle, with isotropic and anisotropic sensing capabilities.

### 4.1 Feedback Robot Motion Planner

Assuming the fully-actuated single-integrator robot dynamics in (4), for a choice of a desired goal location $\mathrm{x}^* \in \mathcal{F}$, we propose a robot navigation strategy, called the "*move-to-projected-goal*" law, $\mathrm{u} : \mathcal{F} \to \mathbb{R}^n$ that steers the robot at location $\mathrm{x} \in \mathcal{F}$ towards the global goal $\mathrm{x}^*$ through the "*projected goal*", $\Pi_{\mathcal{LF}(\mathrm{x})}(\mathrm{x}^*)$, as follows:

$$\mathrm{u}(\mathrm{x}) = -k\big(\mathrm{x} - \Pi_{\mathcal{LF}(\mathrm{x})}(\mathrm{x}^*)\big), \tag{11}$$

where $k \in \mathbb{R}_{>0}$ is a fixed control gain and $\Pi_A$ (5) is the metric projection onto a closed convex set $A \subset \mathbb{R}^n$, and $\mathcal{LF}(\mathrm{x})$ is continuously updated using the Voronoi-adjacent obstacle sensing and its relation with $\mathcal{LW}(\mathrm{x})$ in (10).

Our construction of the "move-to-projected-goal" law in (11) is strongly based on metric projection onto convex sets, which can be efficiently computed using a standard off-the-shelf convex optimization solver Boyd and Vandenberghe (2004). If $\mathcal{W}$ is a convex polytope, then the robot's local free space, $\mathcal{LF}(\mathrm{x})$, is also a convex polytope and can be written as a finite intersection of half-spaces. Hence, the metric projection onto a convex polytope can be recast as a linearly constrained least squares problem and can be solved in polynomial time Kozlov et al. (1980), for example, using active set method Wright and Nocedal (1999), briefly described in Appendix F. In the case of a convex polygonal environment, $\mathcal{LF}(\mathrm{x})$ is a convex polygon and the metric projection onto a convex polygon can be solved analytically, because the solution lies on one of its edges, unless the input point is inside the polygon.

### 4.2 Qualitative Properties

We now continue with a list of certain key qualitative (continuity, existence & uniqueness, invariance and stability) properties of the vector field in (11).

**Proposition 2.** *The "move-to-projected-goal" law in (11) is piecewise continuously differentiable.*

**Proof.** An important property of generalized Voronoi diagrams in (7) inherited from the standard Voronoi diagrams of point generators is that the boundary of each Voronoi cell is a piecewise continuously differentiable function of generator locations Bullo et al. (2009); Rockafellar (1985). In particular, for any $\mathrm{x} \in \mathcal{F}$ the boundary of the robot's local workspace $\mathcal{LW}(\mathrm{x})$ is piecewise continuously differentiable since it is defined by the boundary of the workspace and separating hyperplanes between the robot and obstacles, parametrized by $\mathrm{x}$ and $\Pi_{\overline{O}_i}(\mathrm{x})$, and metric projections onto convex cells are piecewise continuously differentiable Kuntz and Scholtes (1994). Hence, the boundary of the local free space $\mathcal{LF}(\mathrm{x})$ is also piecewise continuously differentiable because $\mathcal{LF}(\mathrm{x})$ is the nonempty erosion of $\mathcal{LW}(\mathrm{x})$ by a fixed open ball. Therefore, one can conclude using the sensitivity analysis of metric projections onto moving convex sets Shapiro (1988); Liu (1995) that the "move-to-projected-goal" law is Lipschitz continuous and piecewise continuously differentiable. ■

**Proposition 3.** *The robot's free space $\mathcal{F}$ in (1) is positively invariant under the "move-to-projected" law (11).*

**Proof.** Since $\mathrm{x}$ and $\Pi_{\mathcal{LF}(\mathrm{x})}(\mathrm{x}^*)$ are both in $\mathcal{LF}(\mathrm{x})$ for any $\mathrm{x} \in \mathcal{F}$, and $\mathcal{LF}(\mathrm{x})$ is an obstacle-free convex neighborhood

of $\mathrm{x}$ (Corollary 1), the line segment joining $\mathrm{x}$ and $\Pi_{\mathcal{LF}(\mathrm{x})}(\mathrm{x}^*)$ is free of collisions. Hence, at the boundary of $\mathcal{F}$, the robot under the "move-to-projected-goal" law either stays on the boundary or moves towards the interior of $\mathcal{F}$, but never crosses the boundary, and so the result follows. ■

**Proposition 4.** *For any initial $\mathrm{x} \in \mathcal{F}$, the "move-to-projected-goal" law (11) has a unique continuously differentiable flow in $\mathcal{F}$ (1) defined for all future time.*

**Proof.** The existence, uniqueness and continuous differentiability of its flow follow from the Lipschitz continuity of the "move-to-projected-goal" law in its compact domain $\mathcal{F}$, because a piecewise continuously differentiable function is locally Lipschitz on its domain Chaney (1990), and a locally Lipschitz function on a compact set is globally Lipschitz on that set Khalil (2001). ■

**Proposition 5.** *The set of stationary points of the "move-to-projected-goal" law (11) is $\{\mathrm{x}^*\} \cup \bigcup_{i=1}^{m} \mathfrak{S}_i$, where*

$$\mathfrak{S}_i := \left\{ \mathrm{x} \in \mathcal{F} \;\middle|\; d(\mathrm{x}, O_i) = r,\ \frac{(\mathrm{x} - \Pi_{\overline{O}_i}(\mathrm{x}))^{\mathrm{T}}(\mathrm{x} - \mathrm{x}^*)}{\|\mathrm{x} - \Pi_{\overline{O}_i}(\mathrm{x})\| \|\mathrm{x} - \mathrm{x}^*\|} = 1 \right\}. \quad (12)$$

**Proof.** It follows from (5) that the goal location $\mathrm{x}^*$ is a stationary point of (11), because $\mathrm{x}^* \in \mathcal{LF}(\mathrm{x}^*)$. In fact, for any $\mathrm{x} \in \mathcal{F}$, one has $\Pi_{\mathcal{LF}(\mathrm{x})}(\mathrm{x}^*) = \mathrm{x}^*$ whenever $\mathrm{x}^* \in \mathcal{LF}(\mathrm{x})$. Hence, in the sequel of the proof, we only consider the set of robot locations satisfying $\mathrm{x}^* \notin \mathcal{LF}(\mathrm{x})$.

Let $\mathrm{x} \in \mathcal{F}$ such that $\mathrm{x}^* \notin \mathcal{LF}(\mathrm{x})$. Recall from (8) and (10) that $\mathcal{LW}(\mathrm{x})$ is determined by the maximum margin separating hyperplanes of the robot body and obstacles, and $\mathcal{LF}(\mathrm{x})$ is obtained by eroding $\mathcal{LW}(\mathrm{x})$ by an open ball of radius $r$. Hence, $\mathrm{x}$ lies in the interior of $\mathcal{LF}(\mathrm{x})$ if and only if $d(\mathrm{x}, O_i) > r$ for all $i$. As a result, since $\mathrm{x}^* \notin \mathcal{LF}(\mathrm{x})$, one has $\mathrm{x} = \Pi_{\mathcal{LF}(\mathrm{x})}(\mathrm{x}^*)$ only if $d(\mathrm{x}, O_i) = r$ for some $i$.

Note that if $d(\mathrm{x}, O_i) = r$, then, since $d(O_i, O_j) > 2r$ (Assumption 1), $d(\mathrm{x}, O_j) > r$ for all $j \neq i$. Therefore, there can be only one obstacle index $i$ such that $\mathrm{x} = \Pi_{\mathcal{LF}(\mathrm{x})}(\mathrm{x}^*)$ and $d(\mathrm{x}, O_i) = r$. Further, given $d(\mathrm{x}, O_i) = r$, since $\Pi_{\mathcal{LF}(\mathrm{x})}(\mathrm{x}^*)$ is the unique closest point of the closed convex set $\mathcal{LF}(\mathrm{x})$ to the goal $\mathrm{x}^*$ (Theorem 2), its optimality Boyd and Vandenberghe (2004) implies that one has $\mathrm{x} = \Pi_{\mathcal{LF}(\mathrm{x})}(\mathrm{x}^*)$ if and only if the maximum margin separating hyperplane between the robot and obstacle $O_i$ is tangent to the level curve of the squared Euclidean distance to the goal, $\|\mathrm{x} - \mathrm{x}^*\|^2$, at $\Pi_{\overline{O}_i}(\mathrm{x})$, and separates $\mathrm{x}$ and $\mathrm{x}^*$, i.e.,

$$\frac{(\mathrm{x} - \Pi_{\overline{O}_i}(\mathrm{x}))^{\mathrm{T}}(\mathrm{x} - \mathrm{x}^*)}{\|\mathrm{x} - \Pi_{\overline{O}_i}(\mathrm{x})\| \|\mathrm{x} - \mathrm{x}^*\|} = 1. \quad (13)$$

Thus, one can locate the stationary points of the "move-to-projected-goal" law in (11) associated with obstacle $O_i$ as in (12), and so the result follows. ■

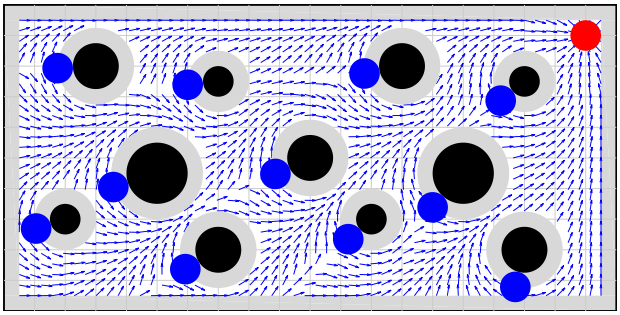

**Fig. 3.** Stationary points of the "move-to-projected-goal" law in (11): there is one unique attractor (red) at the goal location, and there is one saddle point (blue) associated with each obstacle.

Note that, for any equilibrium point $\mathrm{s}_i \in \mathfrak{S}_i$ associated with obstacle $O_i$, one has that the equilibrium $\mathrm{s}_i$, its projection $\Pi_{\overline{O}_i}(\mathrm{s}_i)$ and the goal $\mathrm{x}^*$ are all collinear, see Fig. 3.

**Lemma 2.** *The "move-to-projected-goal" law (11) in a small neighborhood of the goal $\mathrm{x}^*$ is given by*

$$\mathrm{u}(\mathrm{x}) = -k(\mathrm{x} - \mathrm{x}^*), \quad \forall\, \mathrm{x} \in B(\mathrm{x}^*, \epsilon), \quad (14)$$

*for some $\epsilon > 0$; and around any stationary point $\mathrm{s}_i \in \mathfrak{S}_i$ (12), associated with obstacle $O_i$, it is given by*

$$\mathrm{u}(\mathrm{x}) = -k\left(\mathrm{x} - \mathrm{x}^* + \frac{(\mathrm{x} - \Pi_{\overline{O}_i}(\mathrm{x}))^{\mathrm{T}}(\mathrm{x}^* - \mathrm{h}_i)}{\|\mathrm{x} - \Pi_{\overline{O}_i}(\mathrm{x})\|^2}(\mathrm{x} - \Pi_{\overline{O}_i}(\mathrm{x}))\right), \quad (15)$$

*for all $\mathrm{x} \in B(\mathrm{s}_i, \varepsilon)$ and some $\varepsilon > 0$, where*

$$\mathrm{h}_i := \frac{\mathrm{x} + \Pi_{\overline{O}_i}(\mathrm{x})}{2} + \frac{r}{2}\frac{\mathrm{x} - \Pi_{\overline{O}_i}(\mathrm{x})}{\|\mathrm{x} - \Pi_{\overline{O}_i}(\mathrm{x})\|}. \quad (16)$$

**Proof.** See Appendix B.3. ■

Since our "move-to-projected-goal" law strictly decreases the (squared) Euclidean distance to the goal $\mathrm{x}^*$ away from its stationary points (Proposition 7), to guarantee the existence of a unique stable attractor at $\mathrm{x}^*$ we require the following assumption:

**Assumption 2.** *(Obstacle Curvature Condition) The Jacobian matrix $\mathbf{J}_{\Pi_{\overline{O}_i}}(\mathrm{s}_i)$ of the metric projection of any stationary point $\mathrm{s}_i \in \mathfrak{S}_i$ onto the associated obstacle $O_i$ satisfies* [8]

$$\mathbf{J}_{\Pi_{\overline{O}_i}}(\mathrm{s}_i) \prec \frac{\|\mathrm{x}^* - \Pi_{\overline{O}_i}(\mathrm{s}_i)\|}{r + \|\mathrm{x}^* - \Pi_{\overline{O}_i}(\mathrm{s}_i)\|}\mathbf{I} \qquad \forall i, \quad (17)$$

*where $\mathbf{I}$ is the identity matrix of appropriate size.*

In brief, the obstacle curvature condition in Assumption 2 states that at a stationary point $\mathrm{s}_i \in \mathfrak{S}_i$, the associated configuration space (i.e., robot-radius dilated workspace)

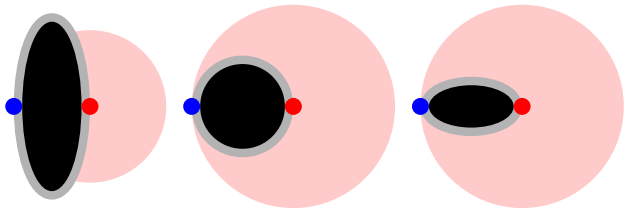

**Fig. 4.** Geometric interpretation of the obstacle curvature condition in Assumption 2. At an unstable stationary point, the associated configuration space (i.e., robot-radius dilated workspace) obstacle should be contained in the enclosing ball of the goal of radius equal to the Euclidean distance of the stationary point to the goal. For the configuration depicted in the left illustration, the obstacle curvature condition fails. Contrarily, for the two contrasting configurations depicted in the middle and right illustrations, the obstacle curvature condition holds true.

obstacle should be contained in the enclosing ball, $B(\mathrm{x}^*, \|\mathrm{s_i} - \mathrm{x}^*\|)$, of the goal of radius equal to the Euclidean distance of the stationary point $\mathrm{s}_i$ to the goal $\mathrm{x}^*$, see Fig. 4 and refer to Appendix C for a detailed geometric interpretation of Assumption 2. For example, the obstacle curvature condition always holds for spherical obstacles, independent of the goal location (Corollary 2). Also note that a similar obstacle curvature condition is necessarily made in the design of navigation functions for spaces with convex obstacles in Filippidis and Kyriakopoulos (2012); Paternain et al. (2017).

**Proposition 6.** *If Assumption 2 holds for the goal* $\mathrm{x}^*$ *and for all obstacles, then* $\mathrm{x}^*$ *is the only locally stable equilibrium of the "move-to-projected-goal" law (11), and all the stationary points,* $\mathrm{s}_i \in \mathfrak{S}_i$ *(12), associated with obstacles,* $O_i$*, are nondegenerate saddles.*

**Proof.** It follows from (14) that the goal $\mathrm{x}^*$ is a locally stable point of the "move-to-projected-goal" law, because its Jacobian matrix, $\mathbf{J}_{\mathrm{u}}(\mathrm{x}^*)$, at $\mathrm{x}^*$ is equal to $-k\,\mathbf{I}$.

Now, to determine the type of any stationary point $\mathrm{s}_i \in \mathfrak{S}_i$ associated with obstacle $O_i$, define

$$g(\mathrm{x}) := \frac{\big(\mathrm{x}^*-\Pi_{\overline{O}_i}(\mathrm{x})\big)^{\mathrm{T}}\big(\mathrm{x}-\Pi_{\overline{O}_i}(\mathrm{x})\big)}{\big\|\mathrm{x}-\Pi_{\overline{O}_i}(\mathrm{x})\big\|^2} - \frac{r}{2\big\|\mathrm{x}-\Pi_{\overline{O}_i}(\mathrm{x})\big\|} - \frac{1}{2}, \tag{18}$$

and so the "move-to-projected-goal" law in a small neighborhood of $\mathrm{s}_i$ in (15) can be rewritten as

$$\mathrm{u}(\mathrm{x}) = -k\Big(\mathrm{x} - \mathrm{x}^* + g(\mathrm{x})\big(\mathrm{x} - \Pi_{\overline{O}_i}(\mathrm{x})\big)\Big). \tag{19}$$

Hence, using $\big\|\mathrm{s}_i-\Pi_{\overline{O}_i}(\mathrm{s}_i)\big\| = r$, one can verify that its Jacobian matrix at $\mathrm{s}_i$ is given by

$$\mathbf{J}_{\mathrm{u}}(\mathrm{s}_i) = -kg(\mathrm{s}_i)\left(\frac{\big\|\mathrm{x}^*-\Pi_{\overline{O}_i}(\mathrm{s}_i)\big\|}{r+\big\|\mathrm{x}^*-\Pi_{\overline{O}_i}(\mathrm{s}_i)\big\|}\mathbf{Q} - \mathbf{J}_{\Pi_{\overline{O}_i}}(\mathrm{s}_i)\right) - \tfrac{k}{2}(\mathbf{I}-\mathbf{Q}), \tag{20}$$

where $g(\mathrm{s}_i) = -\frac{\big\|\mathrm{x}^*-\Pi_{\overline{O}_i}(\mathrm{s}_i)\big\|}{r} - 1 < -2$, and

$$\mathbf{Q} = \mathbf{I} - \frac{\big(\mathrm{s}_i-\Pi_{\overline{O}_i}(\mathrm{s}_i)\big)\big(\mathrm{s}_i-\Pi_{\overline{O}_i}(\mathrm{s}_i)\big)^{\mathrm{T}}}{\big\|\mathrm{s}_i-\Pi_{\overline{O}_i}(\mathrm{s}_i)\big\|^2}. \tag{21}$$

Note that $\mathbf{J}_{\Pi_{\overline{O}_i}}(\mathrm{x})\big(\mathrm{x}-\Pi_{\overline{O}_i}(\mathrm{x})\big) = 0$ for all $\mathrm{x} \in \mathbb{R}^n \setminus \overline{O}_i$ Holmes (1973); Fitzpatrick and Phelps (1982). Hence, if Assumption 2 holds, then one can conclude, from $g(\mathrm{s}_i) < -2$ and (20), that the only negative eigenvalue of $\mathbf{J}_{\mathrm{u}}(\mathrm{s}_i)$ and the associated eigenvector are $-\frac{k}{2}$ and $\big(\mathrm{s}_i - \Pi_{\overline{O}_i}(\mathrm{s}_i)\big)$, respectively; and all other eigenvalues of $\mathbf{J}_{\mathrm{u}}(\mathrm{s}_i)$ are positive. Thus, $\mathrm{s}_i$ is a nondegenerate saddle point of the "move-to-projected-goal" law associated with $O_i$. ■

**Proposition 7.** *Given that the goal location* $\mathrm{x}^*$ *and obstacles satisfy Assumption 2, the goal* $\mathrm{x}^*$ *is an asymptotically stable equilibrium of the "move-to-projected-goal" law (11), whose basin of attraction includes* $\mathcal{F}$*, except a set of measure zero.*[1]

**Proof.** Consider the squared Euclidean distance to the goal as a smooth Lyapunov function candidate, i.e., $V(\mathrm{x}) := \|\mathrm{x} - \mathrm{x}^*\|^2$, and it follows from (5) and (11) that

$$\dot{V}(\mathrm{x}) = -k\underbrace{2(\mathrm{x}-\mathrm{x}^*)^{\mathrm{T}}\big(\mathrm{x}-\Pi_{\mathcal{LF}(\mathrm{x})}(\mathrm{x}^*)\big)}_{\substack{\geq\big\|\mathrm{x}-\Pi_{\mathcal{LF}(\mathrm{x})}(\mathrm{x}^*)\big\|^2 \\ \text{since } \mathrm{x}\in\mathcal{LF}(\mathrm{x}) \text{ and } \|\mathrm{x}-\mathrm{x}^*\|^2\geq\big\|\Pi_{\mathcal{LF}(\mathrm{x})}(\mathrm{x}^*)-\mathrm{x}^*\big\|^2}}, \tag{22}$$

$$\leq -k\big\|\mathrm{x} - \Pi_{\mathcal{LF}(\mathrm{x})}(\mathrm{x}^*)\big\|^2 \leq 0, \tag{23}$$

which is zero iff x is a stationary point. Hence, we have from LaSalle's Invariance Principle Khalil (2001) that all robot configurations in $\mathcal{F}$ asymptotically reach the set of equilibria of (11). Therefore, the result follows from Proposition 2 and Proposition 6, because, under Assumption 2, $\mathrm{x}^*$ is the only stable stationary point of the piecewise continuous "move-to-projected-goal" law (11), and all other stationary points are nondegenerate saddles whose stable manifolds have empty interiors Hirsch et al. (2003). ■

Finally, we find it useful to summarize important qualitative properties of the "move-to-projected-goal" law as:

**Theorem 3.** *The piecewise continuously differentiable "move-to-projected-goal" law in (11) leaves the robot's free space* $\mathcal{F}$ *(1) positively invariant; and if Assumption 2 holds, then its unique continuously differentiable flow, starting at almost*[1] *any configuration* $\mathrm{x} \in \mathcal{F}$*, asymptotically reaches the goal location* $\mathrm{x}^*$*, while strictly decreasing the squared Euclidean distance to the goal,* $\|\mathrm{x} - \mathrm{x}^*\|^2$*, along the way.*

Moreover, since the "move-to-projected-goal" law in (11) is piecewise continously differentiable, it can be

lifted to higher-order dynamical models Koditschek (1987a, 1991); Fierro and Lewis (1997); Arslan and Koditschek (2017). In particular, in Arslan and Koditschek (2017) we show how the invariance and stability properties of the "move-to-projected-goal" law of the first-order (velocity-controlled) robot can be provably extended to the second-order (force-controlled) robot model via reference governors Kolmanovsky et al. (2014).

### 4.3 Extensions for Limited Range Sensing

A crucial property of the "move-to-projected-goal" law (11) is that it only requires the knowledge of the robot's Voronoi-adjacent[3] obstacles to determine the robot's local workspace and so the robot's local free space. We now exploit that property to relax our construction so that it can be put to practical use with commonly available sensors that have bounded radius footprint. This extension results from the construction of the robot's local workspace (8) in terms of the maximum margin separating hyperplanes of convex sets. In consequence, because the intersection of convex sets is convex Boyd and Vandenberghe (2004), perceived obstacles in the robot's (convex) sensory footprint are, in turn, themselves always convex. We will present two specific instances, pointing out along the way how they nevertheless preserve the sufficient conditions for the qualitative properties listed in Section 4.2.

*4.3.1 Navigation using a Fixed Radius Sensory Footprint:* Suppose the robot is equipped with a sensor with a fixed sensing range, $R \in \mathbb{R}_{>0}$, whose sensory output, denoted by $\mathcal{S}_R(\mathrm{x}) := \{S_1, S_2, \ldots, S_m\}$, at a location, $\mathrm{x} \in \mathcal{W}$, returns some computationally effective dense representation of the perceptible portion, $S_i := O_i \cap B(\mathrm{x}, R)$, of each obstacle, $O_i$, in its sensory footprint, $B(\mathrm{x}, R)$. Note that $S_i$ is always open and might possibly be empty (if $O_i$ is outside the robot's sensing range), see Fig. 2(middle); and we assume that the robot's sensing range is greater than the robot body radius, i.e., $R > r$.

As in (8), using the maximum margin separating hyperplanes of the robot and sensed obstacles, we define the robot's *sensed local workspace*, illustrated in Fig. 2(middle), as,

$$\mathcal{LW}_{\mathcal{S}}(\mathrm{x}) := \Big\{ \mathrm{q} \in \mathcal{W} \cap \overline{B\big(\mathrm{x}, \tfrac{r+R}{2}\big)} \;\Big|\; \Big\| \mathrm{q} - \mathrm{x} + r\tfrac{\mathrm{x} - \Pi_{\overline{S}_i}(\mathrm{x})}{\|\mathrm{x} - \Pi_{\overline{S}_i}(\mathrm{x})\|} \Big\| \leq \big\| \mathrm{q} - \Pi_{\overline{S}_i}(\mathrm{x}) \big\|, \forall i \text{ s.t. } S_i \neq \varnothing \Big\}. \quad (24)$$

Note that $\overline{B\big(\mathrm{x}, \frac{r+R}{2}\big)}$ is equal to the intersection of the closed half spaces containing the robot body and defined by the maximum margin separating hyperplanes of the robot body, $\overline{B(\mathrm{x}, r)}$, and all individual points, $\mathrm{q} \in \mathbb{R}^n \setminus B(\mathrm{x}, R)$, outside its sensory footprint. That is to say, the region outside the robot's sensory footprint is assumed to be occupied by obstacles.

An important observation revealing a critical connection between the robot's local workspace $\mathcal{LW}$ in (8) and its sensed local workspace $\mathcal{LW}_{\mathcal{S}}$ in (24) is: For any $\mathrm{x} \in \mathcal{W}$,

**Proposition 8.** $\mathcal{LW}_{\mathcal{S}}(\mathrm{x}) = \mathcal{LW}(\mathrm{x}) \cap \overline{B\big(\mathrm{x}, \frac{r+R}{2}\big)}$.

**Proof.** See Appendix B.4. ■

In accordance with its local free space $\mathcal{LF}(\mathrm{x})$ in (10), we define the robot's *sensed local free space* $\mathcal{LF}_{\mathcal{S}}(\mathrm{x})$ by eroding $\mathcal{LW}_{\mathcal{S}}(\mathrm{x})$ by the robot body, illustrated in Fig. 2(middle), as,

$$\mathcal{LF}_{\mathcal{S}}(\mathrm{x}) := \Big\{ \mathrm{q} \in \mathcal{LW}_{\mathcal{S}}(\mathrm{x}) \Big| \overline{B(\mathrm{q}, r)} \subseteq \mathcal{LW}_{\mathcal{S}}(\mathrm{x}) \Big\}, \quad (25a)$$

$$= \mathcal{LF}(\mathrm{x}) \cap \overline{B\big(\mathrm{x}, \tfrac{R-r}{2}\big)}, \quad (25b)$$

where the latter follows from Proposition 8 and that the erosion operation is distributed over set intersection Haralick et al. (1987). Note that, for any $\mathrm{x} \in \mathcal{F}$, $\mathcal{LF}_{\mathcal{S}}(\mathrm{x})$ is a nonempty closed convex set containing x as is $\mathcal{LF}(\mathrm{x})$.

To safely steer a single-integrator disk-shaped robot in (4) towards a given goal location $\mathrm{x}^* \in \mathcal{F}$ using a fixed radius sensory footprint, we propose the following "move-to-projected-goal" law,

$$\mathrm{u}(\mathrm{x}) = -k\big(\mathrm{x} - \Pi_{\mathcal{LF}_{\mathcal{S}}(\mathrm{x})}(\mathrm{x}^*)\big), \quad (26)$$

where $k > 0$ is a fixed control gain, and $\Pi_{\mathcal{LF}_{\mathcal{S}}(\mathrm{x})}$ (5) is the metric projection onto the robot's sensed local free space $\mathcal{LF}_{\mathcal{S}}(\mathrm{x})$, and $\mathcal{LF}_{\mathcal{S}}(\mathrm{x})$ is assumed to be continuously updated.

Due to the nice relations between the robot's different local neighborhoods in Proposition 8 and (25b), the revised "move-to-projected-goal" law for a fixed radius sensory footprint inherits all qualitative properties of the original one presented in Section 4.2, summarized as:

**Proposition 9.** *The "move-to-projected-goal" law of a disk-shaped robot equipped with a fixed radius sensory footprint in (26) is piecewise continuously differentiable; and if Assumption 2 holds, then its unique continuously differentiable flow asymptotically steers almost[1] all configurations in its positively invariant domain $\mathcal{F}$ towards any given goal location $\mathrm{x}^* \in \mathcal{F}$, while strictly decreasing the (squared) Euclidean distance to the goal along the way.*

**Proof.** The proof of the result follows patterns similar to those of Proposition 2 - Proposition 7, because of the relations between the robot's local neighborhoods in Proposition 8 and (25b), and so it is omitted for the sake of brevity. ■

*4.3.2 Navigation using a 2D LIDAR Range Scanner:* We now present another practical extension of the "move-to-projected-goal" law for safe robot navigation using a 2D LIDAR range scanner in an unknown convex planar environment $\mathcal{W} \subseteq \mathbb{R}^2$ populated with convex obstacles $\mathcal{O} = \{O_1, O_2, \dots, O_m\}$, satisfying Assumption 1. Assuming an angular scanning range of 360 degrees and a fixed radial range of $R \in \mathbb{R}_{>0}$, we model the sensory measurement of the LIDAR scanner at location $\mathrm{x} \in \mathcal{W}$ by a polar curve Stewart (2012) $\rho_{\mathrm{x}} : [-\pi, \pi) \to [0, R]$, defined as,

$$\rho_{\mathrm{x}}(\theta) := \min \begin{pmatrix} R, \\ \min\Big\{ \|\mathrm{p}-\mathrm{x}\| \Big| \mathrm{p} \in \partial\mathcal{W}, \operatorname{atan2}(\mathrm{p}-\mathrm{x}) = \theta \Big\}, \\ \min\limits_i \Big\{ \|\mathrm{p}-\mathrm{x}\| \Big| \mathrm{p} \in O_i, \operatorname{atan2}(\mathrm{p}-\mathrm{x}) = \theta \Big\} \end{pmatrix}. \tag{27}$$

We further assume that the LIDAR sensing range is greater than the robot body radius, i.e., $R > r$.

Suppose $\rho_i : (\theta_{l_i}, \theta_{u_i}) \to [0, R]$ is a convex curve segment of the LIDAR scan $\rho_{\mathrm{x}}$ (27) at location $\mathrm{x} \in \mathcal{W}$ (please refer to Appendix G for the notion of convexity in polar coordinates which we use to identify convex polar curve segments in a LIDAR scan, corresponding to the convex obstacle and workspace boundary), then we define the associated *line-of-sight obstacle* as the open epigraph of $\rho_i$ whose pole is located at x Stewart (2012),

$$L_i := \{\mathrm{x}\} \oplus \mathring{\mathrm{epi}}\rho_i, \tag{28}$$

$$= \{\mathrm{x}\} \oplus \Big\{ (\varrho\cos\theta, \varrho\sin\theta) \Big| \theta \in (\theta_{l_i}, \theta_{u_i}), \varrho > \rho_i(\theta) \Big\}, \tag{29}$$

which is an open convex set. Here, $\mathring{A}$ denotes the interior of a set $A$. Accordingly, we assume the availability of a sensor model $\mathcal{L}_R(\mathrm{x}) := \{L_1, L_2, \dots, L_t\}$ that returns the list of convex line-of-sight obstacles detected by the LIDAR scanner at location x, where $t$ denotes the number of detected obstacles and changes as a function of robot location.

Following the lines of (8) and (10), we define the robot's *line-of-sight local workspace* and *line-of-sight local free space*, illustrated in Fig. 2(right), respectively, as

$$\mathcal{LW}_{\mathcal{L}}(\mathrm{x}) := \Big\{ \mathrm{q} \in L_{ft}(\mathrm{x}) \cap \overline{B\big(\mathrm{x}, \tfrac{r+R}{2}\big)} \Big| \Big\| \mathrm{q} - \mathrm{x} + r\tfrac{\mathrm{x}-\Pi_{\overline{L}_i}(\mathrm{x})}{\|\mathrm{x}-\Pi_{\overline{L}_i}(\mathrm{x})\|} \Big\| \leq \big\| \mathrm{q} - \Pi_{\overline{L}_i}(\mathrm{x}) \big\|, \forall i \Big\}. \tag{30}$$

$$\mathcal{LF}_{\mathcal{L}}(\mathrm{x}) := \Big\{ \mathrm{q} \in \mathcal{LW}_{\mathcal{L}}(\mathrm{x}) \Big| \overline{B(\mathrm{q}, r)} \subseteq \mathcal{LW}_{\mathcal{L}}(\mathrm{x}) \Big\}, \tag{31}$$

where $L_{ft}(\mathrm{x})$ denotes the LIDAR sensory footprint at x, given by the hypograph of the LIDAR scan $\rho_{\mathrm{x}}$ (27) at x, i.e.,

$$L_{ft}(\mathrm{x}) := \{\mathrm{x}\} \oplus \mathrm{hyp}\rho_{\mathrm{x}}, \tag{32}$$

$$= \{\mathrm{x}\} \oplus \Big\{ (\varrho\cos\theta, \varrho\sin\theta) \Big| \theta \in (-\pi, \pi], 0 \leq \varrho \leq \rho_{\mathrm{x}}(\theta) \Big\}. \tag{33}$$

Similar to Proposition 1 and Corollary 1, we have:

**Proposition 10.** *For any $\mathrm{x} \in \mathcal{F}$, $\mathcal{LW}_{\mathcal{L}}(\mathrm{x})$ is an obstacle-free closed convex subset of $\mathcal{W}$ and contains the robot body $B(\mathrm{x}, r)$. Therefore, $\mathcal{LF}_{\mathcal{L}}(\mathrm{x})$ is a nonempty closed convex subset of $\mathcal{F}$ and contains* x.

**Proof.** See Appendix B.5. ■

Accordingly, to navigate a fully-actuated single-integrator robot in (4) using a LIDAR scanner towards a desired goal location $\mathrm{x}^* \in \mathcal{F}$, with the guarantee of no collisions along the way, we propose the following "move-to-projected-goal" law

$$\mathrm{u}(\mathrm{x}) = -k\big(\mathrm{x} - \Pi_{\mathcal{LF}_{\mathcal{L}}(\mathrm{x})}(\mathrm{x}^*)\big), \tag{34}$$

where $k > 0$ is fixed, and $\Pi_{\mathcal{LF}_{\mathcal{L}}(\mathrm{x})}$ (5) is the metric projection onto the robot's line-of-sight free space $\mathcal{LF}_{\mathcal{L}}(\mathrm{x})$ (31), which is assumed to be continuously updated.

We summarize important properties of the "move-to-projected-goal" law for navigation using a 2D LIDAR range scanner as:

**Proposition 11.** *The "move-to-projected-goal" law of a LIDAR-equipped disk-shaped robot in (34) leaves the robot's free space $\mathcal{F}$ (1) positively invariant; and if Assumption 2 holds, then its unique, continuous and piecewise differentiable flow asymptotically brings all but a measure zero set of initial configurations in $\mathcal{F}$ to any designated goal location $\mathrm{x}^* \in \mathcal{F}$, while strictly decreasing the (squared) Euclidean distance to the goal along the way.*

**Proof.** See Appendix B.6. ■

Note that the "move-to-projected-goal" law in (34) might have discontinuities, because of possible occlusions between obstacles. If there is no occlusion between obstacles in the LIDAR's sensing range, then the LIDAR scanner provides exactly the same information about obstacles as does the fixed radius sensory footprint of Section 4.3.1, and so the "move-to-projected-goal" law in (34) is piecewise continuously differentiable as is its version in (26). In this regard, one can avoid occlusions between obstacles by properly selecting the LIDAR's sensing range: for example, since $d(\mathrm{x}, O_i) \geq r$ for any $\mathrm{x} \in \mathcal{F}$ and $d(O_i, O_j) > 2r$ for any $i \neq j$ (Assumption 1), a conservative choice of $R$ that prevents occlusions between obstacles is $r < R \leq 3r$.

Finally, as a practical guide for the effective use of LIDAR range scan, we find it useful to emphasize that a LIDAR range scanner actually behaves as a (finite-resolution) physical sensory solver of metric projection of the robot's centroid onto obstacles, because:

**Lemma 3.** *Each convex polar curve segment (see Appendix G) in a LIDAR scan defines one strict local minimum in the range curve $\rho$ (specifying the closest point*

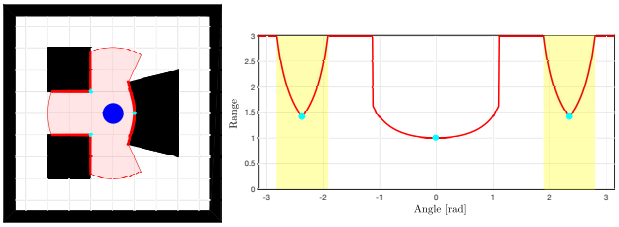


**Fig. 5.** Each convex polar curve segment (highlighted with yellow), associated with convex workspace obstacles, defines a strict local minimum (cyan points) in the LIDAR range scan $\rho$ (red), but a strict local minimum of the range map $\rho$ might be associated with a concave polar curve segment, associated with a concave workspace obstacle.

*of the associated convex line-of-sight obstacle to the robot), but the converse is generally not true, that is to say, a strict local minimum of the range scan might be associated with a concave polar curve segment (i.e., a concave workspace obstacle, as illustrated in Fig. 5).*

**Proof.** The result follows from the fact that each convex polar curve segment defines a convex line-of-sight obstacle in the workspace and the closest point of a convex set to a given point, i.e., metric projection, is unique (Theorem 2). See Fig. 5 for an example where the converse fails. ■

Therefore, since we here only consider convex workspace obstacles, in our numerical and experimental implementations using a LIDAR scanner, we directly use the strict local minima of a range scan to compute the local workspace and the local free space in (30) and (31), respectively.

### 4.4 An Extension for Differential Drive Robots

Maintaining the specialization to the plane, $\mathcal{W} \subset \mathbb{R}^2$, we now consider a disk-shaped differential drive robot described by state $(\mathrm{x}, \theta) \in \mathcal{F} \times [-\pi, \pi)$, centered at $\mathrm{x} \in \mathcal{F}$ with body radius $r \in \mathbb{R}_{>0}$ and orientation $\theta \in [-\pi, \pi)$, moving in $\mathcal{W}$. The kinematic equations describing its motion are

$$\dot{\mathrm{x}} = v \begin{bmatrix} \cos\theta \\ \sin\theta \end{bmatrix}, \quad \text{and} \quad \dot{\theta} = \omega, \tag{35}$$

where $v \in \mathbb{R}$ and $\omega \in \mathbb{R}$ are, respectively, the linear (tangential) and angular velocity inputs of the robot.

In contrary to the "move-to-projected-goal" law of a fully actuated robot in (11), a differential drive robot can not directly move towards the projected goal $\Pi_{\mathcal{LF}(\mathrm{x})}(\mathrm{x}^*)$ of a given goal location $\mathrm{x}^* \in \mathring{\mathcal{F}}$, unless it is perfectly aligned with $\Pi_{\mathcal{LF}(\mathrm{x})}(\mathrm{x}^*)$, because it is underactuated due to the nonholonomic constraint $\begin{bmatrix} -\sin\theta \\ \cos\theta \end{bmatrix}^{\mathrm{T}} \dot{\mathrm{x}} = 0$. [9] In consequence, to determine the robot's linear motion, we restrict the robot's local free space $\mathcal{LF}(\mathrm{x})$ (10) to conform to the nonholonomic constraint as

$$\mathcal{LF}_v(\mathrm{x}, \theta) := \mathcal{LF}(\mathrm{x}) \cap H_N, \tag{36}$$

where

$$H_N := \left\{ \mathrm{x} + \nu \begin{bmatrix} \cos\theta \\ \sin\theta \end{bmatrix} \middle| \, \nu \in \mathbb{R} \right\} \tag{37}$$

is the straight line motion range due to the nonholonomic constraint. Note that $\mathcal{LF}(\mathrm{x}) \cap H_N$ is a closed line segment in $\mathcal{W}$ and contains x. Similarly, to determine the robot's angular motion, we define

$$\mathcal{LF}_\omega(\mathrm{x}) := \mathcal{LF}(\mathrm{x}) \cap H_G, \tag{38}$$

where

$$H_G := \left\{ \lambda \mathrm{x} + (1-\lambda)\mathrm{x}^* \in \mathbb{R}^2 \middle| \, \lambda \in \mathbb{R} \right\} \tag{39}$$

is the line going through x and $\mathrm{x}^*$.

Accordingly, based on a standard differential drive controller Astolfi (1999), we propose the following "move-to-projected-goal" law for a differential drive robot, [10] [11]

$$v = -k \begin{bmatrix} \cos\theta \\ \sin\theta \end{bmatrix}^{\mathrm{T}} \left( \mathrm{x} - \Pi_{\mathcal{LF}_v(\mathrm{x},\theta)}(\mathrm{x}^*) \right), \tag{40a}$$

$$\omega = k \operatorname{atan}\left( \frac{\begin{bmatrix} -\sin\theta \\ \cos\theta \end{bmatrix}^{\mathrm{T}} \left( \mathrm{x} - \frac{\Pi_{\mathcal{LF}_\omega(\mathrm{x})}(\mathrm{x}^*) + \Pi_{\mathcal{LF}(\mathrm{x})}(\mathrm{x}^*)}{2} \right)}{\begin{bmatrix} \cos\theta \\ \sin\theta \end{bmatrix}^{\mathrm{T}} \left( \mathrm{x} - \frac{\Pi_{\mathcal{LF}_\omega(\mathrm{x})}(\mathrm{x}^*) + \Pi_{\mathcal{LF}(\mathrm{x})}(\mathrm{x}^*)}{2} \right)} \right), \tag{40b}$$

where $k > 0$ is fixed, and $\mathcal{LF}_v(\mathrm{x}, \theta)$, $\mathcal{LF}_\omega(\mathrm{x})$ and $\mathcal{LF}(\mathrm{x})$ are assumed to be continuously updated. Here, we follow Astolfi (1999) by resolving the indeterminacy through setting $\omega = 0$ whenever $\mathrm{x} = \frac{\Pi_{\mathcal{LF}_\omega(\mathrm{x})}(\mathrm{x}^*) + \Pi_{\mathcal{LF}(\mathrm{x})}(\mathrm{x}^*)}{2}$. Note that this introduces the discontinuity necessitated by Brockett's condition Brockett (1983).

We summarize some important properties of the "move-to-projected-goal" law of a differential drive robot as:

**Proposition 12.** *Given the goal and obstacles satisfy Assumption 2, the "move-to-projected-goal" law of a disk-shaped differential drive robot in (40) asymptotically steers almost[1] all configurations in its positively invariant domain $\mathcal{F} \times [-\pi, \pi)$ towards any given goal location $\mathrm{x}^* \in \mathring{\mathcal{F}}$, without increasing the Euclidean distance to the goal along the way.*

**Proof.** See Appendix B.7. ■

Note that the "move-to-projected-goal" law of a differential drive robot in (40) can be extended to limited range sensing models by using the robot's sensed local free space $\mathcal{LF}_\mathcal{S}$ (25) or the robot's line-of-sight local free space $\mathcal{LF}_\mathcal{L}$ (31) instead of the local free space $\mathcal{LF}$ (10), and the resulting vector field planner maintains qualitative properties.

### 4.5 An Extension for Differential Drive Robots with Anisotropic LIDAR Range Scanners

Consider a disk-shaped differential drive robot, represented by state $(\mathrm{x},\theta)\in\mathcal{F}\times[-\pi,\pi)$ and evolving according to (35) as described in Section 4.4, equipped with an anisotropic LIDAR range scanner of angular sensing range strictly less than 360 degrees, whose range measurements, at a robot configuration $(\mathrm{x},\theta)$, are represented by a polar curve $\rho_{\mathrm{x},\theta}:[-\alpha,\alpha]\to[0,R]$ defined as

$$\rho_{\mathrm{x},\theta}(\phi):=\rho_{\mathrm{x}}(\phi\boxplus\theta), \tag{41}$$

where $0<2\alpha<2\pi$ is the angular sensing range of the LIDAR scanner in radians, $R>0$ is the LIDAR's radial sensing range, and $\rho_{\mathrm{x}}$ is the range map defined in (27). Here, to ensure the interval $[-\pi,\pi)$ of radians, the addition and subtraction operations of radians are defined as

$$\phi\boxplus\theta:=\mod(\phi+\theta+\pi,2\pi)-\pi, \tag{42}$$
$$\phi\boxminus\theta:=\mod(\phi-\theta+\pi,2\pi)-\pi, \tag{43}$$

where $\mod(a,b)$ denotes $a$ modulo $b$, i.e., the remainder of the division of $a$ by $b$. Following an opportunistic approach, we find it convenient to define an extended range map $\hat{\rho}_{\mathrm{x}}:[-\pi,\pi)\to[0,R]$ as

$$\hat{\rho}_{\mathrm{x}}(\varphi):=\begin{cases}\rho_{\mathrm{x},\theta}(\varphi\boxminus\theta) & \text{, if } \varphi\boxminus\theta\in[-\alpha,\alpha],\\ R & \text{, otherwise,}\end{cases} \tag{44}$$
$$=\begin{cases}\rho_{\mathrm{x}}(\varphi) & \text{, if } \varphi\boxminus\theta\in[-\alpha,\alpha],\\ R & \text{, otherwise,}\end{cases} \tag{45}$$

which assumes that the unseen region of the workspace by the anisotropic LIDAR sensor is empty. Notice that the anisotropic range map $\rho_{\mathrm{x},\theta}$ is defined in the robot's body coordinates, whereas the extended range map $\hat{\rho}_{\mathrm{x}}$ is defined in the global configuration coordinates.

By construction, the anisotropic LIDAR scanner cannot observe some portion of the workspace behind the robot, because its sensing direction is well-aligned with the forward direction of the differential drive robot. Hence, to ensure safe navigation, we restrict our differential drive robot to move only in forward direction, where the robot's forward motion range that is consistent with the nonholonomic constraint is given by

$$H_F:=\left\{\mathrm{x}+\nu\begin{bmatrix}\cos\theta\\ \sin\theta\end{bmatrix}\,\middle|\,\nu\geq 0\right\}. \tag{46}$$

Now, following the lines of Section 4.3.2 and using the the extended range map $\hat{\rho}_{\mathrm{x}}$ in (44), one can construct the robot's line-of-sight local free space $\mathcal{LF}_{\mathcal{L}}(\mathrm{x})$ as described in (31). Moreover, as in (36) and (38), we define the local free spaces for linear and angular motion as

$$\mathcal{LF}_{\mathcal{L}\,v}(\mathrm{x},\theta):=\mathcal{LF}_{\mathcal{L}}(\mathrm{x})\cap H_F, \tag{47}$$
$$\mathcal{LF}_{\mathcal{L}\,\omega}(\mathrm{x}):=\mathcal{LF}_{\mathcal{L}}(\mathrm{x})\cap H_G, \tag{48}$$

where $H_G$ in (39) is the line passing through the robot position x and the goal $\mathrm{x}^*$. Accordingly, to navigate towards a given goal location $\mathrm{x}^*\in\mathring{\mathcal{F}}$, we propose the following "move-to-projected-goal" law specifying the linear, $v$, and the angular, $\omega$, velocity inputs for a forward-moving differential robot with an anisotropic LIDAR sensor,

$$v=-k\begin{bmatrix}\cos\theta\\ \sin\theta\end{bmatrix}^{\mathrm{T}}\left(\mathrm{x}-\Pi_{\mathcal{LF}_{\mathcal{L}\,v}(\mathrm{x},\theta)}(\mathrm{x}^*)\right), \tag{49a}$$

$$\omega=k\,\mathrm{atan2}\left(\begin{bmatrix}-\sin\theta\\ \cos\theta\end{bmatrix}^{\mathrm{T}}\left(\mathrm{x}-\frac{\Pi_{\mathcal{LF}_{\mathcal{L}\,\omega}(\mathrm{x})}(\mathrm{x}^*)+\Pi_{\mathcal{LF}_{\mathcal{L}}(\mathrm{x})}(\mathrm{x}^*)}{2}\right),\right.$$
$$\left.\begin{bmatrix}\cos\theta\\ \sin\theta\end{bmatrix}^{\mathrm{T}}\left(\mathrm{x}-\frac{\Pi_{\mathcal{LF}_{\mathcal{L}\,\omega}(\mathrm{x})}(\mathrm{x}^*)+\Pi_{\mathcal{LF}_{\mathcal{L}}(\mathrm{x})}(\mathrm{x}^*)}{2}\right)\right), \tag{49b}$$

where $k>0$ is a fixed control gain. Note that, by construction, the linear velocity $v$ is nonnegative and so always yields forward motion.

The "move-to-projected-goal" law in (49) for a forward moving differential drive robot with an anisotropic LIDAR sensor inherits all the qualitative properties from the associated versions in (34) and (40) presented in Section 4.3.2 and Section 4.4, respectively, as long as the LIDAR's angular scanning range is 180 degrees:

**Proposition 13.** *Given that the goal and obstacles satisfy Assumption 2, the "move-to-projected-goal" law of a forward moving disk-shaped differential drive robot with an anisotropic LIDAR scanner in (49) has no stationary points other than the locations specified by Proposition 5, and asymptotically brings almost[1] all initial conditions in $\mathcal{F}\times[-\pi,\pi)$ to any given goal location $\mathrm{x}^*\in\mathring{\mathcal{F}}$ with no collisions along the way if and only if the LIDAR's angular scanning range is 180 degrees, i.e., $2\alpha=\pi$.*

**Proof.** See Appendix B.8. ■

## 5 2D Navigable Environments for a Greedy Robotic Agent

In this section, we address the properties of planar convex sphere world environments, considered as fixed configurations of convex obstacles, that afford distance-diminishing reactive navigation to arbitrarily chosen goals in the free space. Here, "reactive navigation" denotes any Lipschitz continuous vector field whose flow is positive invariant on and whose basin around the asymptotically stable goal point comprises almost all of the environment. The term "distance-diminishing," the property that the Euclidean norm to the chosen destination is non-increasing along all trajectories of the resulting flow, represents our intuitive notion of a "greedy" algorithm. The "move-to-projected-goal" law in (11) offers one example of such a greedy reactive navigation rule for environments that satisfy Assumption 2 in Section 4.2 relative to a specific choice of goal. The question now arises whether that assumption

is overly restrictive. We will show, contrarily, that this assumption is not merely sufficient but also necessary for greedy navigation. In consequence, it turns out that any environment possessing a distance-diminishing reactive navigation law whose designated goal may be placed at will in the free space must have obstacles that are not merely convex but also "round" in a sense to be made precise below.

Before proceeding, it is convenient to introduce some additional terminology.

**Definition 2** A fully-actuated first-order robotic agent, moving towards a goal location $\mathrm{x}^* \in \mathcal{F}$ according to a safe Lipschitz continuous navigation policy $\mathrm{u}_{\mathrm{x}^*} : \mathcal{F} \to \mathbb{R}^n$, i.e.,

$$\dot{\mathrm{x}} = \mathrm{u}_{\mathrm{x}^*}(\mathrm{x}), \tag{50}$$

is said to be *distance-diminishing* iff the Euclidean distance of the robot to the goal is nonincreasing along the navigation trajectory, i.e.,

$$\nabla_{\mathrm{x}} \|\mathrm{x} - \mathrm{x}^*\|^2 \cdot \mathrm{u}_{\mathrm{x}^*}(\mathrm{x}) \leq 0. \tag{51}$$

It is straightforward to observe that such a greedy robotic agent cannot achieve (almost) global reactive navigation in a planar environment punctured by any nonconvex obstacle. We now develop a further necessary condition on convex obstacles that is required to assure the capability of such a greedy navigation agent to reach arbitrarily placed goals.

**Definition 3** A convex planar set with twice differentiable boundary is said to be *round* iff the center of curvature (i.e., the center of the osculating circle) at any boundary point is contained in the set itself.

For example, an ellipsoid of aspect ratio (the ratio of the major axis to the minor axis) less than 2 (e.g., a disk) is a round convex set.

**Proposition 14.** *In a planar convex sphere world with isolated obstacles (Assumption 1), if a distance-diminishing reactive navigation policy can reach arbitrarily placed goals in free space then all configuration space (i.e., robot-radius dilated workspace) obstacles are round.*

**Proof.** Proof by contrapositive. Suppose $\widehat{O}_i$ be a configuration space obstacle, obtained by dilating the workspace obstacle $O_i$ with the robot radius $r$, that is not round. Then, there exists a boundary point $\mathrm{x} \in \partial\widehat{O}_i$ of $\widehat{O}_i$ at which the center of curvature $\mathrm{c}$ lies outside $\widehat{O}_i$. Now consider a point $\mathrm{x}^* \in \mathcal{F}$ that is located strictly in between the boundary point $\mathrm{x}$ and its center of curvature $\mathrm{c}$, which is guaranteed to exist because $\mathrm{c} \notin \widehat{O}_i$. Since $\|\mathrm{x} - \mathrm{c}\| > \|\mathrm{x} - \mathrm{x}^*\|$, the balls $B(\mathrm{c}, \|\mathrm{x} - \mathrm{c}\|)$ and $B(\mathrm{x}^*, \|\mathrm{x} - \mathrm{x}^*\|)$ are tangent at $\mathrm{x}$ and satisfy $B(\mathrm{x}^*, \|\mathrm{x} - \mathrm{x}^*\|) \subsetneq B(\mathrm{c}, \|\mathrm{x} - \mathrm{c}\|)$. Hence, there does not exist a collision-free path in $\mathcal{F}$ from $\mathrm{x}$ to $\mathrm{x}^*$ along which the distance to $\mathrm{x}^*$ is nonincreasing. Due to continuity, this holds for a small neighborhood of $\mathrm{x}$, and so a distance-diminishing robotic agent cannot reach to $\mathrm{x}^*$ starting from this set of nonzero measure. Thus, the result follows. ■

**Theorem 4.** *In a planar convex sphere world, the move-to-projected-goal law in (11) guarantees safe navigation towards any free space goal configuration starting from almost[1] any initial configurations if and only if all configuration space obstacles are round.*

**Proof.** The necessity of obstacles being round follows from Proposition 14. The sufficiency of obstacles being round follows from that a round obstacle satisfies the curvature condition in Assumption 2, which can be verified using Proposition 5, Proposition 15 and Lemma 9. ■

An interesting research question that we leave open for a future study is that how these results on planar navigable environments extend to higher dimensions. It is not difficult to convince oneself that a greedy robotics agent can navigate around isolated configuration space obstacles that can be written as a cross product of round planar sets or all of whose 2D cross-sections are round; for instance, sphere, torus or unbounded cylinder are navigable obstacles for a greedy robotic agent Filippidis and Kyriakopoulos (2012).

## 6 Numerical Simulations

To demonstrate the motion pattern generated by our "move-to-projected-goal" law around and far away from the goal, we consider a $10 \times 10$ and a $50 \times 10$ environment cluttered with convex obstacles and a desired goal located at around the upper right corner, as illustrated in Fig. 6 and Fig. 7, respectively. [12] We present in these figures example navigation trajectories of the "move-to-projected-goal" law for different sensing and actuation modalities. We observe a significant consistency between the resulting trajectories of the "move-to-projected-goal" law and the boundary of the Voronoi diagram of the environment, where the robot balances its distance to all proximal obstacles while navigating towards its destination — a desired autonomous behaviour for many practical settings instead of following the obstacle boundary tightly. In our simulations, we avoid occlusions between obstacles by properly selecting the LIDAR's sensing range, and in so doing both limited range sensing models provide the same information about the environment away from the workspace boundary and the associated "move-to-projected-goal" laws yield almost the same navigation paths. As observed in Fig. 6, although they are initiated at the same location, a fully actuated and a differential drive robot may follow significantly different trajectories due to their differences in system dynamics and controller design. It is also useful to note that the "move-to-projected-goal" law decreases not only the Euclidean

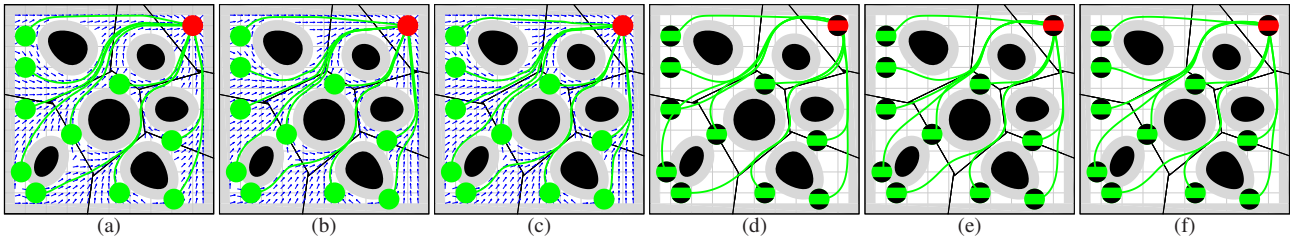


**Fig. 6.** Example navigation trajectories of the "move-to-projected-goal" law starting at a set of initial configurations (green) towards a designated point goal (red) for different sensing and actuation models: (a,b,c) a fully actuated robot, (d,e,f) a differential drive robot, (a,d) Voronoi-adjacent[3] obstacle sensing, (b,e) a fixed radius sensory footprint, (c,f) a limited range LIDAR sensor. Also see Extension 1 for the resultant motion.

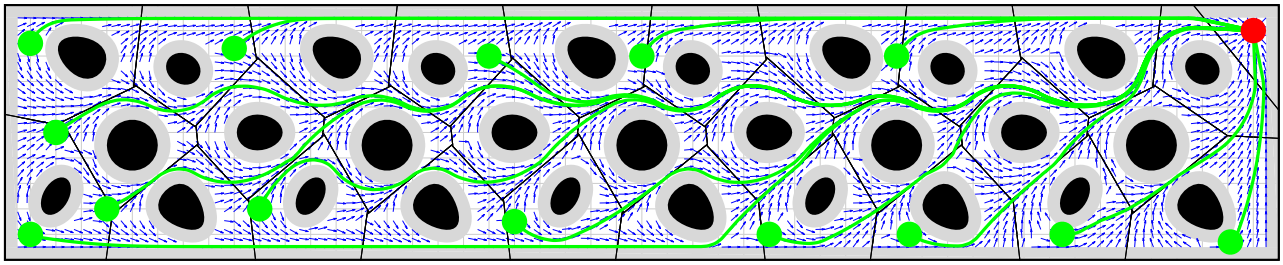

**Fig. 7.** Example navigation trajectories of the "move-to-projected-goal" law in (11) starting at a set of initial positions (green) far away from the goal (red). Also see Extension 2 and refer to Appendix I for additional figures illustrating the navigation pattern far away from the goal for different sensing and actuation models

distance, $\|\mathrm{x}-\mathrm{x}^*\|$, to the goal, but also the Euclidean distance, $\left\|\Pi_{\mathcal{LF}(\mathrm{x})}(\mathrm{x}^*)-\mathrm{x}^*\right\|$, between the projected goal, $\Pi_{\mathcal{LF}(\mathrm{x})}(\mathrm{x}^*)$, and the global goal, $\mathrm{x}^*$, illustrated in Fig. 8.

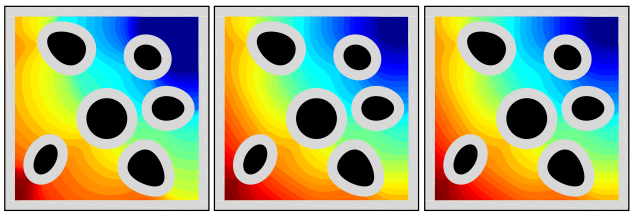

**Fig. 8.** The Euclidean distance, $\left\|\Pi_{\mathcal{LF}(\mathrm{x})}(\mathrm{x}^*)-\mathrm{x}^*\right\|$, between the projected goal, $\Pi_{\mathcal{LF}(\mathrm{x})}(\mathrm{x}^*)$, and the global goal, $\mathrm{x}^*$, for different sensing modalities: (left) Voronoi-adjacent[3] obstacle sensing, (middle) a fixed radius sensory footprint, (right) a limited range line-of-sight sensor.

## 7 Experimental Validation

For experimental validation of the proposed "move-to-projected-goal" law, we set up a 8m×4m environment cluttered with eight cylindrical obstacles of radius ( 0.1m and 0.3m) and introduce a TurtleBot 2 platform[13] equipped with a Hokuyo UTM-30LX scanning rangefinder[14], illustrated in Fig. 9 (top). We use a Vicon motion capture system[15] for ground truth measurements: it tracks the robotic platform in real time at 100Hz and localizes workspace obstacles as well as registering (and visualizing) designated initial and goal locations, thereby offering the flexibility to test and record experiments involving arbitrary configurations of obstacles and source-destination goals. During our experiments with the Hokuyo UTM-30LX 40Hz LIDAR scanner, we limit the measurement range from maximum range 30m to 2m (due to the workspace limits) and the angular scanning range from 270° to 180° (due to Proposition 13), and the local free space is constructed using the local minima of range measurements, as described in Section 4.3.2 (see Lemma 3) and Section 4.5, after smoothing with a five-point Gaussian moving average filter with the unit variance Szeliski (2011). To eliminate higher-order dynamical effects, we limit the velocity of the TurtleBot 2 platform from its maximum speed of 0.65m/s to 0.45m/s, and we model the robot body as a disk of radius 0.3m (with 0.05m safety clearance). We implement our navigation algorithms in Python[16], running onboard vector field updates at better than 100Hz, and manage our experiments using Robot Operating System (ROS)[17] with onboard robot motion control updates at 20Hz. In the experiments now reported, we always start up our platform at around the same "right-hand bottom" corner of the workspace depicted in Fig. 9 (denoted by the black and blue striped disk), and then command it to sequentially visit a varied array of initial positions (denoted by cyan disks) from each of which it must then navigate towards a fixed designated goal position (denoted by the red disk).

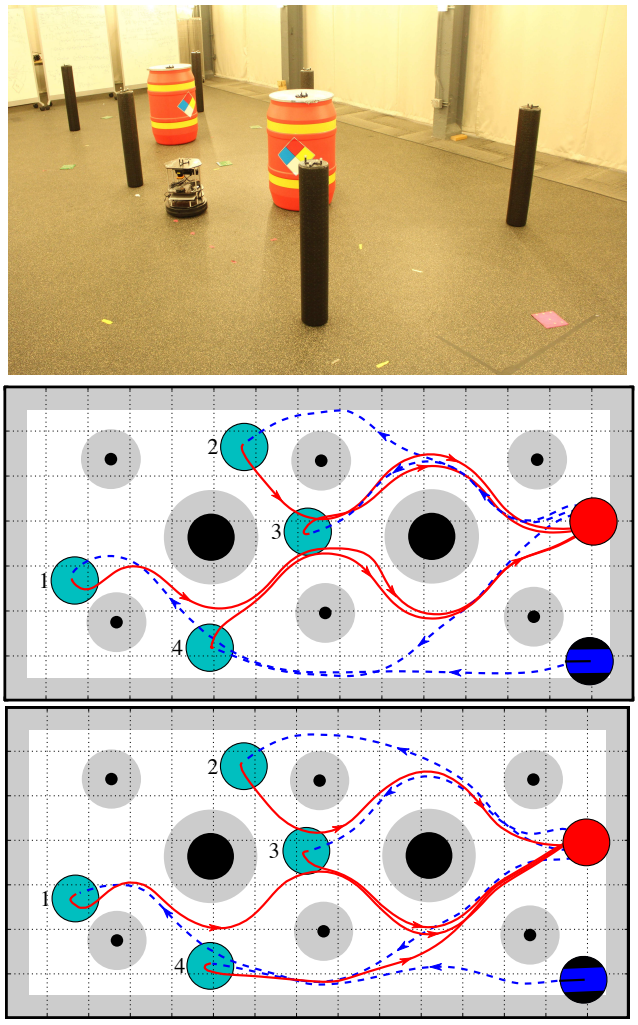


**Fig. 9.** (top) Experimental setup: a TurtleBot 2 platform equipped with a Hokuyo UTM-30LX range scanner navigates around cylindrical (depicted as black circles in the figures below) obstacles (physical black foam rollers and red barrels as viewed in the photo) from a set of initial (cyan) positions towards a goal (red) location. (center) Navigation using Voronoi-adjacent obstacle sensing via motion capture, (bottom) Navigation using anisotropic 2D LIDAR range scans delivered in real time (40Hz) by the Hokuyo device. Also see Extension 3 and Extension 4 for the full motion.

In our first set of experiments, we test the "move-to-projected-goal" law in (40) for the (forward-moving [11]) differential drive robot model using Voronoi-adjacent[3] obstacle sensing via motion capture. In the second set of experiments, we test the "move-to-projected-goal" law in (49) for the (forward-moving) differential drive robot model with an anisotropic range scanner. Fig. 9 (center)-(bottom), respectively, depicts the resulting navigation trajectories for these two different experimental settings. As expected, the two different sensing models yield distinctly different local free space estimates, resulting in significantly different navigation paths from the same set of initial conditions relative to the fixed problem (i.e. obstacle-goal) configuration. It is also worth remarking that the navigation trajectories from goal to start, and from start to goal often exhibit different homotopy classes (i.e., with respect to the projected position coordinates on the punctured plane) since the navigation policy is a function of both robot position and orientation. Moreover, as suggested by Fig. 6 and Fig. 9, these experimental studies conducted at speeds consistent with the presumed "first order unicycle" robot dynamics model exhibit very little gap between theory and practice. Throughout these trials, we observe a similar motion pattern: the robot balances its distance to perceived environmental clutter while moving towards its destination.

## 8 Conclusions

In this paper we construct a sensor-based feedback law that solves the real-time collision-free robot navigation problem in a domain cluttered with convex obstacles. Our algorithm introduces a novel use of separating hyperplanes for identifying the robot's local obstacle-free convex neighborhood, affording a piecewise smooth velocity command instantaneously pointing towards the metric projection of the designated goal location onto this convex set. Given separated and appropriately "strongly" convex obstacles, we show that the resulting vector field has a smooth flow with a unique attractor at the goal location (along with the topologically inevitable saddles — at least one for each obstacle). Since all of its critical points are nondegenerate, our vector field asymptotically steers almost all configurations in the robot's free space to the goal, with the guarantee of no collisions along the way. We also present its practical extensions for limited range isotropic and anisotropic sensing models and the widely used differential drive model, while maintaining formal guarantees. We illustrate the effectiveness of the proposed navigation algorithm in numerical simulations and experimental studies.

Work now in progress targets a fully smoothed version of the move-to-projected-goal law (by recourse to reference governors Kolmanovsky et al. (2014)), permitting its lift to more complicated dynamical models such as force-controlled (second order) and more severely underactuated systems Arslan and Koditschek (2017). This will enable its empirical demonstration for safe, high-speed navigation in a forest-like environments Vasilopoulos et al. (2017) and in dynamic human crowds. We are also investigating the extension of these ideas for coordinated, decentralized feedback control of multirobot swarms. Another exciting research direction is combining a discrete-time version of the "move-to-projected-goal" law (Appendix H) with a (e.g., sampling-based) motion planning algorithm to

solve online robot navigation problem in complex high-dimensional configuration space Arslan et al. (2017).

## Appendix A
## Index to Multimedia Extensions

**Table 1.** Index to Multimedia Extensions

| Extension | Media Type | Description |
|---|---|---|
| 1 | Video | General framework and numerical simulations |
| 2 | Video | Motion pattern far away from goal |
| 3 | Video | Experimental validation |
| 4 | Video | Chasing a moving goal |

## Appendix B
## Proofs

### B.1 Proof of Lemma 1

**Proof.** By definition (5), the metric projection $\Pi_{\overline{A}}(\mathrm{x})$ of the ball's centroid $\mathrm{x}$ onto the convex set $\overline{A}$ is the unique closest point of $\overline{A}$ to $\mathrm{x}$. Hence, due to the symmetry of the ball, the closest point of $\overline{B(\mathrm{x},r)}$ to $\overline{A}$ lies on the line segment joining $\mathrm{x}$ and $\Pi_{\overline{A}}(\mathrm{x})$, and is given by $(\Pi_{\overline{B(\mathrm{x},r)}} \circ \Pi_{\overline{A}})(\mathrm{x}) = \mathrm{x} - r\frac{\mathrm{x}-\Pi_{\overline{A}}(\mathrm{x})}{\|\mathrm{x}-\Pi_{\overline{A}}(\mathrm{x})\|}$, and so the closest point of $\overline{A}$ to $\overline{B(\mathrm{x},r)}$ is $\Pi_{\overline{A}}(\mathrm{x})$. Thus, the result follows. ■

### B.2 Proof of Proposition 1

**Proof.** To prove the result, it is convenient to rewrite (8) as $\mathcal{LW}(\mathrm{x}) = \mathcal{W} \cap \bigcap_i HS_i$, where

$$HS_i := \left\{ \mathrm{q} \in \mathbb{R}^n \,\middle|\, \left\| \mathrm{q} - \mathrm{x} + r\frac{\mathrm{x}-\Pi_{\overline{O}_i}(\mathrm{x})}{\|\mathrm{x}-\Pi_{\overline{O}_i}(\mathrm{x})\|} \right\| \leq \left\| \mathrm{q} - \Pi_{\overline{O}_i}(\mathrm{x}) \right\| \right\}. \quad (52)$$

Note that for any $\mathrm{x} \in \mathcal{F}$, $HS_i$ is the half space defined by the maximum margin separating hyperplane between the robot body $\overline{B(\mathrm{x},r)}$ and obstacle $O_i$ (Lemma 1), and contains the robot. Moreover, since $O_i$ is open, we have $O_i \cap HS_i = \varnothing$ for any $\mathrm{x} \in \mathcal{F}$.

Hence, using (1), one can verify the result as follows:

$$\mathrm{x} \in \mathcal{F} \iff \begin{cases} \overline{B(\mathrm{x},r)} \subseteq \mathcal{W}, \\ \overline{B(\mathrm{x},r)} \cap O_i = \varnothing \quad \forall i, \end{cases} \quad (53)$$

$$\iff \begin{cases} \overline{B(\mathrm{x},r)} \subseteq \mathcal{W}, \\ \overline{B(\mathrm{x},r)} \subseteq HS_i \quad \forall i, \\ O_i \cap HS_i = \varnothing \quad \forall i, \end{cases} \quad (54)$$

$$\iff \begin{cases} \overline{B(\mathrm{x},r)} \subseteq \mathcal{LW}(\mathrm{x}), \\ O_i \cap \mathcal{LW}(\mathrm{x}) = \varnothing \quad \forall i, \end{cases} \quad (55)$$

which completes the proof. ■

### B.3 Proof of Lemma 2

**Proof.** The result for the goal location $\mathrm{x}^*$ follows from the continuity of Voronoi diagrams in (7) and $\mathrm{x}^* \in \mathcal{LF}(\mathrm{x}^*)$.

To see the result for any stationary point $\mathrm{s}_i \in \mathfrak{S}_i$, recall from the proof of Proposition 5 that $\mathrm{s}_i$ lies on the boundary segment of $\mathcal{LF}(\mathrm{s}_i)$ defined by the separating hyperplane between the robot and $i$th obstacle, and $\mathrm{s}_i$ has a certain nonzero clearance from the boundary segment of $\mathcal{LF}(\mathrm{s}_i)$ defined by the separating hyperplane between the robot and any other obstacle. Hence, using the continuity of Voronoi diagrams, for any $\mathrm{x} \in B(\mathrm{s}_i, \varepsilon)$ the "projected-goal" $\Pi_{\mathcal{LF}(\mathrm{x})}(\mathrm{x}^*)$ can be located by taking the projection of $\mathrm{x}^*$ onto (a shifted version of) the maximum margin separating hyperplane between the robot and $i$th obstacle as

$$\Pi_{\mathcal{LF}(\mathrm{x})}(\mathrm{x}^*) = \mathrm{x}^* - \frac{\left(\mathrm{x}-\Pi_{\overline{O}_i}(\mathrm{x})\right)^{\mathrm{T}}(\mathrm{x}^*-\mathrm{h}_i)}{\left\|\mathrm{x}-\Pi_{\overline{O}_i}(\mathrm{x})\right\|^2}\left(\mathrm{x}-\Pi_{\overline{O}_i}(\mathrm{x})\right), \quad (56)$$

where $\mathrm{h}_i$ is defined as in (16), and so this completes the proof. ■

### B.4 Proof of Proposition 8

**Proof.** As discussed in the proof of Proposition 1, for any $\mathrm{x} \in \mathcal{W}$ we have $\mathcal{LW}(\mathrm{x}) = \mathcal{W} \cap \bigcap_i HS_i$, where $HS_i$ is defined as in (52). Similarly, one can rewrite (24) as $\mathcal{LW}_{\mathbb{S}}(\mathrm{x}) = \mathcal{W} \cap \overline{B\left(\mathrm{x}, \frac{r+R}{2}\right)} \cap \bigcap_i \widehat{HS}_i$, where

$$\widehat{HS}_i := \left\{ \mathrm{q} \in \mathbb{R}^n \,\middle|\, \left\| \mathrm{q} - \mathrm{x} + r\frac{\mathrm{x}-\Pi_{\overline{S}_i}(\mathrm{x})}{\|\mathrm{x}-\Pi_{\overline{S}_i}(\mathrm{x})\|} \right\| \leq \left\| \mathrm{q} - \Pi_{\overline{S}_i}(\mathrm{x}) \right\| \right\}. \quad (57)$$

Note that if $S_i = \varnothing$, then the predicate in (57) is trivially holds and so $\widehat{HS}_i = \mathbb{R}^n$; otherwise, since $S_i = O_i \cap B(\mathrm{x}, R)$, we have $\Pi_{\overline{S}_i}(\mathrm{x}) = \Pi_{\overline{O}_i}(\mathrm{x})$ and so $\widehat{HS}_i = HS_i$. Moreover, if $S_i = \varnothing$ (i.e., $d(\mathrm{x}, O_i) > R$), then we also have from Definition 1 and Lemma 1 that $\overline{B\left(\mathrm{x}, \frac{r+R}{2}\right)} \subset HS_i$. Thus, we obtain that

$$\widehat{HS}_i \cap \overline{B\left(\mathrm{x}, \tfrac{r+R}{2}\right)} = HS_i \cap \overline{B\left(\mathrm{x}, \tfrac{r+R}{2}\right)}, \quad \forall i. \quad (58)$$

Therefore, one can verify the result as follows:

$$\mathcal{LW}_{\mathbb{S}}(\mathrm{x}) = \mathcal{W} \cap \overline{B\left(\mathrm{x}, \tfrac{r+R}{2}\right)} \cap \bigcap_i \widehat{HS}_i, \quad (59)$$

$$= \mathcal{W} \cap \bigcap_i \left( \widehat{HS}_i \cap \overline{B\left(\mathrm{x}, \tfrac{r+R}{2}\right)} \right), \quad (60)$$

$$= \mathcal{W} \cap \bigcap_i \left( HS_i \cap \overline{B\left(\mathrm{x}, \tfrac{r+R}{2}\right)} \right), \quad (61)$$

$$= \left( \mathcal{W} \cap \bigcap_i HS_i \right) \cap \overline{B\left(\mathrm{x}, \tfrac{r+R}{2}\right)}, \quad (62)$$

$$= \mathcal{LW}(\mathrm{x}) \cap \overline{B\left(\mathrm{x}, \tfrac{r+R}{2}\right)}. \quad (63)$$

■

### *B.5 Proof of Proposition 10*

**Proof.** For any $\mathrm{x} \in \mathcal{F}$, the LIDAR sensory footprint in (32) can be equivalently rewritten using the global knowledge of the robot's workspace as

$$L_{ft}(\mathrm{x}) = \mathcal{W} \cap \overline{B(\mathrm{x}, R)} \setminus \bigcup_i A_i. \tag{64}$$

where $A_i$ is the augmented line-of-sight obstacle associated with obstacle $O_i$, defined as

$$A_i := \Big\{ \alpha(\mathrm{p}-\mathrm{x})+\mathrm{p} \Big| \mathrm{p} \in O_i, \alpha \in [0,\infty) \Big\}. \tag{65}$$

Hence, since $R > r$, it follows from (30) that

$$\mathcal{LW}_{\mathcal{L}}(\mathrm{x}) = \widehat{\mathcal{LW}}_{\mathcal{L}}(\mathrm{x}) \setminus \bigcup_i A_i, \tag{66}$$

where

$$\widehat{\mathcal{LW}}_{\mathcal{L}}(\mathrm{x}) := \Big\{ \mathrm{q} \in \mathcal{W} \cap \overline{B\big(\mathrm{x}, \tfrac{r+R}{2}\big)} \Big| \Big\| \mathrm{q} - \mathrm{x} + r \tfrac{\mathrm{x}-\Pi_{\overline{L_i}}(\mathrm{x})}{\|\mathrm{x}-\Pi_{\overline{L_i}}(\mathrm{x})\|} \Big\| \leq \big\| \mathrm{q} - \Pi_{\overline{L_i}}(\mathrm{x}) \big\|, \forall i \Big\}. \tag{67}$$

Note that, as discussed in the proof of Proposition 1, since $\mathrm{x} \in \mathcal{F}$, $\widehat{\mathcal{LW}}_{\mathcal{L}}(\mathrm{x})$ is a closed convex set and free of any line-of-sight obstacle $L_i$, i.e., $\widehat{\mathcal{LW}}_{\mathcal{L}}(\mathrm{x}) \cap L_i = \varnothing$ for all $i$; and it contains the robot body, i.e., $\overline{B(\mathrm{x}, r)} \subseteq \widehat{\mathcal{LW}}_{\mathcal{L}}(\mathrm{x})$.

Now observe that if obstacle $O_i$ is in the LIDAR's sensing range, i.e, $O_i \cap B(\mathrm{x}, R) \neq \varnothing$, then $A_i \cap B(\mathrm{x}, R) = L_j \cap B(\mathrm{x}, R)$ for some $j$. Hence, since $\widehat{\mathcal{LW}}_{\mathcal{L}}(\mathrm{x})$ is free of line-of-sight obstacles, we have from (66) that $\mathcal{LW}_{\mathcal{L}}(\mathrm{x}) = \widehat{\mathcal{LW}}_{\mathcal{L}}(\mathrm{x})$. Thus, the result follows since $\mathcal{LF}_{\mathcal{L}}(\mathrm{x})$ is the erosion of $\mathcal{LW}_{\mathcal{L}}(\mathrm{x})$ by the robot body radius $r$. ■

### *B.6 Proof of Proposition 11*

**Proof.** As discussed in the proof of Proposition 3, the positive invariance of $\mathcal{F}$ under the "move-to-projected-goal" law in (34) follows from that for any $\mathrm{x} \in \mathcal{F}$ the robot's line-of-sight local free space $\mathcal{LF}_{\mathcal{L}}(\mathrm{x})$ (31) is an obstacle-free closed convex subset of $\mathcal{F}$, and contains both $\mathrm{x}$ and $\Pi_{\mathcal{LF}_{\mathcal{L}}(\mathrm{x})}(\mathrm{x}^*)$ (Proposition 10 and Theorem 2). Hence, $-k\big(\mathrm{x}-\Pi_{\mathcal{LF}_{\mathcal{L}}(\mathrm{x})}(\mathrm{x}^*)\big) \in T_{\mathrm{x}}\mathcal{F}$ is either interior directed or, at worst, tangent to the boundary of $\mathcal{F}$.

The existence, uniqueness and continuity of its flow can be observed using a partitioning of $\mathcal{F}$ such that the "move-to-projected-goal" law is piecewise continuously differentiable in each connected component of any partition element. Let $D_t$ denote the set of collision free robot locations at which the number of detected line-of-sight obstacles is equal to $t \in \mathbb{N}$, i.e.,

$$D_t := \big\{ \mathrm{x} \in \mathcal{F} \,\big|\, \big|\mathcal{L}_R(x)\big| = t \big\}. \tag{68}$$

Recall that $\mathcal{L}_R(x) = \{L_1, L_2, \ldots, L_t\}$ is our sensor model that returns the list of convex line-of-sight obstacles detected by the LIDAR at location $\mathrm{x}$. Hence, the collection of $D_t$'s defines a partition of $\mathcal{F}$.

Now observe that $D_t$ is generally disconnected and the "move-to-projected-goal" law is piecewise continuously differentiable when its domain is restricted to any connected component of $D_t$ since each line-of-sight obstacle is associated with an open convex segment of a LIDAR scan and each connected component of $D_t$ is uniquely associated with a certain collection of obstacles and workspace boundary segments. Hence, since a piecewise continuously differentiable function is Lipschitz continuous on a compact set Chaney (1990); Khalil (2001), the "move-to-projected-goal" law has a unique continuously differentiable flow in every connected component of $D_t$. Further, when the robot enters a connected component of $D_t$, it stays in that connected component for a nonzero time since a line-of-sight obstacle $L_i$ is an open set and can not instantaneously appear or disappear under any continuous motion. Thus, the unique, continuous and piecewise differentiable flow of the move-to-projected-goal" law in $\mathcal{F}$ is constructed by piecing together its unique, continuously differentiable trajectories in every connected component of $D_t$'s.

Finally, using a similar pattern to the proofs of Proposition 5 and Proposition 6, one can verify that the set of stationary points of (34) is $\{\mathrm{x}^*\} \cup \bigcup_{i=1}^{m} \mathfrak{S}_i$, where $\mathfrak{S}_i$ is defined as in (12); and if Assumption 2 holds, then the goal $\mathrm{x}^*$ is the only locally stable point of (34), and all the stationary points, $\mathfrak{S}_i$, associated with obstacles, $O_i$, are nondegenerate saddles. Moreover, as discussed in the proof of Proposition 7, the "move-to-projected-goal" law in (34) strictly decreases the (squared) Euclidean distance to $\mathrm{x}^*$ away from its stationary points, and so $\mathrm{x}^*$ is the unique attractor of (34) whose basin of attraction includes all but a measure zero set of $\mathcal{F}$. ■

### *B.7 Proof of Proposition 12*

**Proof.** The positive invariance of $\mathcal{F} \times (-\pi, \pi]$ under the "move-to-projected-goal" law (40) and the existence and uniqueness of its flow can be established using similar patterns of the proofs of Proposition 2, Proposition 3 and Proposition 4, and the flow properties of the differential drive controller in Astolfi (1999).

As in the proof of Proposition 7, using the squared distance to goal, $V(\mathrm{x}) = \|\mathrm{x}-\mathrm{x}^*\|^2$, as a smooth Lypunov function, one can verify the stability properties from (5), (35), and (40) as follows: for any $(\mathrm{x}, \theta) \in \mathcal{F} \times (-\pi, \pi]$

$$\dot{V}(\mathrm{x}) = -k \underbrace{2(\mathrm{x}-\mathrm{x}^*)^{\mathrm{T}}\big(\mathrm{x}-\Pi_{\mathcal{LF}_v(\mathrm{x},\theta)}(\mathrm{x}^*)\big)}_{\geq \left\|\mathrm{x}-\Pi_{\mathcal{LF}_v(\mathrm{x},\theta)}(\mathrm{x}^*)\right\|^2 \text{ since } \mathrm{x} \in \mathcal{LF}_v(\mathrm{x},\theta) \text{ and } \|\mathrm{x}-\mathrm{x}^*\|^2 \geq \left\|\Pi_{\mathcal{LF}_v(\mathrm{x},\theta)}(\mathrm{x}^*)-\mathrm{x}^*\right\|^2}, \tag{69}$$

$$\leq -k\left\|\mathrm{x}-\Pi_{\mathcal{LF}_v(\mathrm{x},\theta)}(\mathrm{x}^*)\right\|^2 \leq 0. \tag{70}$$

Hence, it follows from LaSalle Invariance Principle Khalil (2001) that all configurations in $\mathcal{F}\times(-\pi,\pi]$ asymptotically reach the set of configurations where robots are located at the associated projected goal $\Pi_{\mathcal{LF}_v(\mathrm{x},\theta)}(\mathrm{x}^*)$ at any arbitrary orientation,

$$\left\{(\mathrm{x},\theta)\in\mathcal{F}\times(-\pi,\pi]\middle|\mathrm{x}=\Pi_{\mathcal{LF}_v(\mathrm{x},\theta)}(\mathrm{x}^*)\right\}. \tag{71}$$

Note that for any fixed $\Pi_{\mathcal{LF}_v(\mathrm{x},\theta)}(\mathrm{x}^*)$, $\Pi_{\mathcal{LF}_\omega(\mathrm{x})}(\mathrm{x}^*)$ and $\Pi_{\mathcal{LF}(\mathrm{x})}(\mathrm{x}^*)$, the standard differential drive controller asymptotically aligns the robot's direction toward $\frac{\Pi_{\mathcal{LF}_\omega(\mathrm{x})}(\mathrm{x}^*)+\Pi_{\mathcal{LF}(\mathrm{x})}(\mathrm{x}^*)}{2}$, i.e.,

$$\begin{bmatrix}-\sin\theta\\ \cos\theta\end{bmatrix}^{\mathrm{T}}\left(\mathrm{x}-\frac{\Pi_{\mathcal{LF}_\omega(\mathrm{x})}(\mathrm{x}^*)+\Pi_{\mathcal{LF}(\mathrm{x})}(\mathrm{x}^*)}{2}\right)=0. \tag{72}$$

Hence, using the optimality of metric projection in (5) one can conclude that $\Pi_{\mathcal{LF}_v(\mathrm{x},\theta)}(\mathrm{x}^*)=\Pi_{\mathcal{LF}_\omega(\mathrm{x})}(\mathrm{x}^*)=\Pi_{\mathcal{LF}(\mathrm{x})}(\mathrm{x}^*)$ whenever $\mathrm{x}=\Pi_{\mathcal{LF}_v(\mathrm{x},\theta)}(\mathrm{x}^*)$ and $\begin{bmatrix}-\sin\theta\\ \cos\theta\end{bmatrix}^{\mathrm{T}}\left(\mathrm{x}-\frac{\Pi_{\mathcal{LF}_\omega(\mathrm{x})}(\mathrm{x}^*)+\Pi_{\mathcal{LF}(\mathrm{x})}(\mathrm{x}^*)}{2}\right)=0$.

Therefore, using a similar approach as the proofs of Proposition 5, Lemma 2 and Proposition 6, one can verify that the set of stationary points of (40) is given by

$$\{\mathrm{x}^*\}\times(-\pi,\pi]\bigcup\left\{(\mathrm{s}_i,\theta)\in\mathcal{F}\times(-\pi,\pi]\middle|\mathrm{s}_i\in\mathfrak{S}_i,\begin{bmatrix}-\sin\theta\\ \cos\theta\end{bmatrix}^{\mathrm{T}}(\mathrm{s}_i-\mathrm{x}^*)=0\right\}, \tag{73}$$

where $\mathfrak{S}_i$ is defined as in (12); and every robot configuration located at $\mathrm{x}^*$ is locally stable and all stationary points associated with obstacles are nondegenerate saddles with stable manifolds of measure zero. Thus, the result follows. ■

## B.8 Proof of Proposition 13

**Proof.** Since our forward moving differential drive robot has a symmetric disk-shaped body and the LIDAR scanning window is symmetric with respect to the robot's forward direction, safe navigation requires at least an angular scanning range of 180 degrees. In the rest of the proof, we will show that to eliminate any spurious stationary points, the LIDAR's angular scanning range should be less than or equal to 180 degrees. Therefore, the result directly follows from Proposition 11 and Proposition 12.

First, by definition (31), we always have that if the robot is away from the stationary points specified by Proposition 5, then $\mathrm{x}\in\mathring{\mathcal{LF}}_{\mathcal{L}}(\mathrm{x})$. Hence, if the robot is relatively aligned with the goal, i.e., $\begin{bmatrix}\cos\theta\\ \sin\theta\end{bmatrix}^{\mathrm{T}}(\mathrm{x}^*-\mathrm{x})>0$, then the robot's linear velocity is always nonzero, because $\mathrm{x}\neq\Pi_{\mathcal{LF}_{\mathcal{L}v}(\mathrm{x},\theta)}(\mathrm{x}^*)$. Thus, there cannot be any spurious stationary point if $\begin{bmatrix}\cos\theta\\ \sin\theta\end{bmatrix}^{\mathrm{T}}(\mathrm{x}^*-\mathrm{x})>0$.

Otherwise, i.e., $\begin{bmatrix}\cos\theta\\ \sin\theta\end{bmatrix}^{\mathrm{T}}(\mathrm{x}^*-\mathrm{x})\leq 0$, due to the forward motion constraint, the robot's linear velocity is zero at any position in the free space $\mathcal{F}$ and the robot turns in place to asymptotically align with $\frac{\Pi_{\mathcal{LF}_{\mathcal{L}\omega}(\mathrm{x})}(\mathrm{x}^*)+\Pi_{\mathcal{LF}_{\mathcal{L}}(\mathrm{x})}(\mathrm{x}^*)}{2}$. Since $\mathcal{LF}_{\mathcal{L}v},\mathcal{LF}_{\mathcal{L}\omega}\subset\mathcal{LF}_L$, asymptotic alignment with $\frac{\Pi_{\mathcal{LF}_{\mathcal{L}_\omega}(\mathrm{x})}(\mathrm{x}^*)+\Pi_{\mathcal{LF}_{\mathcal{L}}(\mathrm{x})}(\mathrm{x}^*)}{2}$ guarantees that the robot relatively aligns with the goal (i.e., $\begin{bmatrix}\cos\theta\\ \sin\theta\end{bmatrix}^{\mathrm{T}}(\mathrm{x}^*-\mathrm{x})>0$) in finite time, and continue moving towards its destination. Hence, the only issue that might happen during turn-in-place motion is an undesired sign change in the angular velocity due to some appearing and disappearing obstacles perceived at around the angular limits of the LIDAR sensor.

Note that if the global goal $\mathrm{x}^*$ is behind the robot, i.e., $\begin{bmatrix}\cos\theta\\ \sin\theta\end{bmatrix}^{\mathrm{T}}(\mathrm{x}^*-\mathrm{x})\leq 0$, then the angular motion goal $\frac{\Pi_{\mathcal{LF}_{\mathcal{L}\omega}(\mathrm{x})}(\mathrm{x}^*)+\Pi_{\mathcal{LF}_{\mathcal{L}}(\mathrm{x})}(\mathrm{x}^*)}{2}$ is also behind the robot, i.e., $\begin{bmatrix}\cos\theta\\ \sin\theta\end{bmatrix}^{\mathrm{T}}\left(\frac{\Pi_{\mathcal{LF}_{\mathcal{L}_\omega}(\mathrm{x})}(\mathrm{x}^*)+\Pi_{\mathcal{LF}_{\mathcal{L}}(\mathrm{x})}(\mathrm{x}^*)}{2}-\mathrm{x}\right)\leq 0$. Hence, $\frac{\Pi_{\mathcal{LF}_{\mathcal{L}_\omega}(\mathrm{x})}(\mathrm{x}^*)+\Pi_{\mathcal{LF}_{\mathcal{L}}(\mathrm{x})}(\mathrm{x}^*)}{2}$ is located either on the second or third quadrant of the robot's body coordinate frame. A newly appearing or disappearing obstacle along the LIDAR's scanning angle limits introduces or removes a separating hyperplane constraint and so reshapes the local free space $\mathcal{LF}_{\mathcal{L}}(\mathrm{x})$, which, depending on the LIDAR's angular sensing range, might cause a jump of $\frac{\Pi_{\mathcal{LF}_{\mathcal{L}_\omega}(\mathrm{x})}(\mathrm{x}^*)+\Pi_{\mathcal{LF}_{\mathcal{L}}(\mathrm{x})}(\mathrm{x}^*)}{2}$ from the second quadrant to the third quadrant or vise versa, causing a sign change in the angular velocity control $\omega$ in (49).

If the LIDAR's angular scanning range is less than or equal to 180 degrees, i.e., $2\alpha\leq\pi$, then such a chance in separating hyperplane constraints defining $\mathcal{LF}_{\mathcal{L}}(\mathrm{x})$ cannot cause a chance in the sign of $\omega$, because the added or removed separating hyperplane never crosses the boundary of the second and the third quadrants of the robot's body coordinate frame. Whereas, if the LIDAR's angular scanning range is greater then 180 degrees, i.e., $2\alpha>\pi$, then the chance in separating hyperplane constraints shaping $\mathcal{LF}_{\mathcal{L}}(\mathrm{x})$ can cause a sign change in $\omega$ because the associated hyperplane always crosses the boundary of the second and third quadrants of the robot's body frame and can cause a sudden jump of $\frac{\Pi_{\mathcal{LF}_{\mathcal{L}_\omega}(\mathrm{x})}(\mathrm{x}^*)+\Pi_{\mathcal{LF}_{\mathcal{L}}(\mathrm{x})}(\mathrm{x}^*)}{2}$ between these quadrants. Thus, the sign chance in $\omega$ can be avoided only if the LIDAR's angular scanning range is less than or equal to $\pi$, which completes the proof. ■

## Appendix C
## Geometric Interpretation of the Obstacle Curvature Condition

A convenient way of characterizing metric limitations, such as the obstacle curvature condition in Assumption 2, of the "move-to-projected-goal" law is in terms of the enclosing balls of the goal $\mathrm{x}^*$, defined as:

**Definition 4** The *enclosing ball*, $B_{\mathrm{x}} := B(\mathrm{x}^*, \|\mathrm{x}-\mathrm{x}^*\|-r)$, of the goal $\mathrm{x}^*$ associated with a robot location $\mathrm{x} \in \mathbb{R}^n \setminus B(\mathrm{x}^*, r)$ is the largest open ball, centered at $\mathrm{x}^*$, that does not intersect with the robot body $\overline{B(\mathrm{x}, r)}$.

In other words, the enclosing ball $B_{\mathrm{x}}$ is the largest ball centered at the goal $\mathrm{x}^*$ such that a disk-shaped robot of radius $r$ starting at location $\mathrm{x}$ can go around it without increasing the Euclidean distance to the goal.

Observe that for any stationary point $\mathrm{s}_i \in \mathfrak{S}_i$ (12) associated with obstacle $O_i$, one has $B_{\mathrm{s}_i} = B\big(\mathrm{x}^*, \big\|\mathrm{x}^* - \Pi_{\overline{O}_i}(\mathrm{s}_i)\big\|\big)$ and $\Pi_{\overline{B}_{\mathrm{s}_i}}(\mathrm{s}_i) = \Pi_{\overline{O}_i}(\mathrm{s}_i)$, because $\mathrm{s}_i$, $\Pi_{\overline{O}_i}(\mathrm{s}_i)$ and $\mathrm{x}^*$ are all collinear (Proposition 5). That is to say, $B_{\mathrm{s}_i}$ is tangent to (i.e, the osculating ball of) $O_i$ at $\Pi_{\overline{O}_i}(\mathrm{s}_i)$. Hence, we have

$$\Pi_{\overline{B}_{\mathrm{s}_i}}(\mathrm{x}) = \big\|\mathrm{x}^* - \Pi_{\overline{O}_i}(\mathrm{s}_i)\big\| \frac{\mathrm{x}-\mathrm{x}^*}{\|\mathrm{x}-\mathrm{x}^*\|} \quad \forall \mathrm{x} \in \mathbb{R}^n \setminus \overline{B}_{\mathrm{s}_i}, \tag{74}$$

and so the Jacobian matrix $\mathbf{J}_{\Pi_{\overline{B}_{\mathrm{s}_i}}}(\mathrm{s}_i)$ of the metric projection of $\mathrm{s}_i$ onto the associated enclosing ball $B_{\mathrm{s}_i}$ is given by

$$\mathbf{J}_{\Pi_{\overline{B}_{\mathrm{s}_i}}}(\mathrm{s}_i) = \frac{\big\|\mathrm{x}^* - \Pi_{\overline{O}_i}(\mathrm{s}_i)\big\|}{r + \big\|\mathrm{x}^* - \Pi_{\overline{O}_i}(\mathrm{s}_i)\big\|} \mathbf{Q}_i(\mathrm{s}_i), \tag{75}$$

where

$$\mathbf{Q}_i(\mathrm{x}) := \mathbf{I} - \frac{\big(\mathrm{x} - \Pi_{\overline{O}_i}(\mathrm{x})\big)\big(\mathrm{x} - \Pi_{\overline{O}_i}(\mathrm{x})\big)^{\mathrm{T}}}{\big\|\mathrm{x} - \Pi_{\overline{O}_i}(\mathrm{x})\big\|^2}, \quad \forall \mathrm{x} \in \mathbb{R}^n \setminus \overline{O}_i. \tag{76}$$

Therefore, since $\mathbf{Q}_i(\mathrm{s}_i) \preccurlyeq \mathbf{I}$, one can conclude that the upper bound in (17) of Assumption 2 is due to the enclosing ball $B_{\mathrm{s}_i}$ of the goal $\mathrm{x}^*$ associated with $\mathrm{s}_i$. Because any path starting at $\mathrm{x} \in \mathbb{R}^n$ along which the distance to the goal $\mathrm{x}^*$ is strictly decreasing should stay in $B_{\mathrm{x}}$ for all future time; and the "move-to-projected-goal" law yields such navigation paths (Theorem 3).

More precisely, the geometric connection between enclosing balls of the goal and the curvature condition in Assumption 2 can be established as follows:

**Proposition 15.** *Let $\mathrm{s}_i \in \mathfrak{S}_i$ (12) be a critical point associated with obstacle $O_i$. If $\overline{O}_i \setminus \Pi_{\overline{O}_i}(\mathrm{s}_i) \subset B_{\mathrm{s}_i}$, then*

$$\mathbf{J}_{\Pi_{\overline{O}_i}}(\mathrm{s}_i) \prec \frac{\big\|\mathrm{x}^* - \Pi_{\overline{O}_i}(\mathrm{s}_i)\big\|}{\big\|\mathrm{x}^* - \Pi_{\overline{O}_i}(\mathrm{s}_i)\big\| + r} \mathbf{I}. \tag{77}$$

*Therefore, if $\overline{O}_i \setminus \Pi_{\overline{O}_i}(\mathrm{s}_i) \subset B_{\mathrm{s}_i}$ for all $i \in \{1, 2, \ldots, m\}$ and $\mathrm{s}_i \in \mathfrak{S}_i$, then Assumption 2 holds.*

**Proof.** Since $\Pi_{\overline{B}_{\mathrm{s}_i}}(\mathrm{s}_i) = \Pi_{\overline{O}_i}(\mathrm{s}_i)$, the result can be verified using a similar pattern of the proof of Lemma 9; here the only difference is that the entire $\overline{O}_i$, except $\Pi_{\overline{O}_i}(\mathrm{s}_i)$, is strictly contained in $B_{\mathrm{s}_i}$. ■

Alternatively, using functional representations of obstacles, one can verify Assumption 2 as follows:

**Proposition 16.** *Let each obstacle $O_i$ be associated with a convex function $f_i : \mathbb{R}^n \to \mathbb{R}$ such that $O_i = f_i^{-1}(-\infty, c_i)$ for some $c_i \in \mathbb{R}$. Then, Assumption 2 holds if*

$$\frac{\nabla^2 f_i\big(\Pi_{\overline{O}_i}(\mathrm{s}_i)\big)}{\big\|\nabla f_i\big(\Pi_{\overline{O}_i}(\mathrm{s}_i)\big)\big\|} \succ \frac{1}{\big\|\mathrm{x}^* - \Pi_{\overline{O}_i}(\mathrm{s}_i)\big\|}, \tag{78}$$

*for all $i \in \{1, 2, \ldots, m\}$ and $\mathrm{s}_i \in \mathfrak{S}_i$ (12).*

**Proof.** Consider the enclosing ball $B_{\mathrm{s}_i}$ of the goal $\mathrm{x}^*$ associated with $\mathrm{s}_i \in \mathfrak{S}_i$. We have from Definition 4 that $B_{\mathrm{s}_i} = \beta^{-1}\big(-\infty, \big\|\mathrm{x}^* - \Pi_{\overline{O}_i}(\mathrm{s}_i)\big\|\big)$, where $\beta(\mathrm{x}) := \|\mathrm{x}-\mathrm{x}^*\|^2$. Hence, it follows that

$$\frac{\nabla^2 \beta\Big(\Pi_{\overline{B}_{\mathrm{s}_i}}(\mathrm{s}_i)\Big)}{\Big\|\nabla \beta\Big(\Pi_{\overline{B}_{\mathrm{s}_i}}(\mathrm{s}_i)\Big)\Big\|} = \frac{1}{\big\|\mathrm{x}^* - \Pi_{\overline{O}_i}(\mathrm{s}_i)\big\|}. \tag{79}$$

Thus, since $\Pi_{\overline{B}_{\mathrm{s}_i}}(\mathrm{s}_i) = \Pi_{\overline{O}_i}(\mathrm{s}_i)$, one can conclude the result from Lemma 7 and Lemma 8. ■

Two immediate corollaries of Proposition 15 and Proposition 16 for the case of spherical and ellipsoidal obstacles are:

**Corollary 2.** *If all obstacles are open balls, then Assumption 2 holds for any goal $\mathrm{x}^* \in \mathcal{F}$.*

**Corollary 3.** *Let each obstacle $O_i$ be an open ellipsoid defined as $O_i = f_i^{-1}(-\infty, c_i)$ for some $c_i \in \mathbb{R}$, where $f_i := (\mathrm{x} - \mathrm{p}_i)^{\mathrm{T}} \mathbf{A}_i (\mathrm{x} - \mathrm{p}_i)$ and $\mathbf{A}_i \in \mathbb{R}^{n \times n}$ is symmetric positive definite. Then, Assumption 2 holds if*

$$\frac{\lambda_{\min}(\mathbf{A}_i)}{\lambda_{\max}(\mathbf{A}_i)} > \frac{\big\|\mathrm{p}_i - \Pi_{\overline{O}_i}(\mathrm{s}_i)\big\|}{\big\|\mathrm{x}^* - \Pi_{\overline{O}_i}(\mathrm{s}_i)\big\|}, \tag{80}$$

*for all $i \in \{1, 2, \ldots m\}$ and $\mathrm{s}_i \in \mathfrak{S}_i$, where $\lambda_{\min}(\mathbf{A}_i)$ and $\lambda_{\max}(\mathbf{A}_i)$ are, respectively, the minimum and maximum eigenvalues of $\mathbf{A}_i$.*

**Proof.** The results follows from Proposition 16 and

$$\frac{\nabla^2 f_i\big(\Pi_{\overline{O}_i}(\mathrm{s}_i)\big)}{\big\|\nabla f_i\big(\Pi_{\overline{O}_i}(\mathrm{s}_i)\big)\big\|} = \frac{\mathbf{A}}{\big\|\mathbf{A}\big(\mathrm{p}_i - \Pi_{\overline{O}_i}(\mathrm{s}_i)\big)\big\|}, \tag{81}$$

$$\succcurlyeq \frac{\lambda_{\min}(\mathbf{A}_i)}{\lambda_{\max}(\mathbf{A}_i)} \frac{1}{\big\|\mathrm{p}_i - \Pi_{\overline{O}_i}(\mathrm{s}_i)\big\|} \mathbf{I}. \tag{82}$$

■

In consequence, one can briefly conclude that it is easier for a robot to navigate around obstacles more spherical (i.e., not too flat) and towards goal locations away from obstacles, while strictly decreasing the Euclidean distance to the goal.

## Appendix D
## Uniqueness of Maximum Margin Separating Hyperplanes

For any two disjoint convex sets $A, B \in \mathbb{R}^n$, there can be more than one pair of points $\mathrm{a} \in \overline{A}$ and $\mathrm{b} \in \overline{B}$ achieving $\|\mathrm{a}-\mathrm{b}\| = d(A,B)$; however, they all have the same maximum margin separating hyperplane:

**Lemma 4.** *Let $A, B \subset \mathbb{R}^n$ be two disjoint convex sets, and $\mathrm{a}_1, \mathrm{a}_2 \in A$ and $\mathrm{b}_1, \mathrm{b}_2 \in B$ be points with $\|\mathrm{a}_1-\mathrm{b}_1\| = \|\mathrm{a}_2-\mathrm{b}_2\| = d(A,B)$. Then, for any $\mathrm{x} \in \mathbb{R}^n$, the following equality always holds*

$$(\mathrm{a}_1-\mathrm{b}_1)^{\mathrm{T}}\left(\mathrm{x}-\frac{\mathrm{a}_1+\mathrm{b}_1}{2}\right) = (\mathrm{a}_2-\mathrm{b}_2)^{\mathrm{T}}\left(\mathrm{x}-\frac{\mathrm{a}_2+\mathrm{b}_2}{2}\right). \quad (83)$$

**Proof.** First, to see that $\mathrm{a}_1 - \mathrm{b}_1 = \mathrm{a}_2 - \mathrm{a}_2$, consider

$$\begin{aligned}(\mathrm{a}_1-\mathrm{b}_1)^{\mathrm{T}}(\mathrm{a}_2-\mathrm{b}_2) &= (\mathrm{a}_1-\mathrm{b}_1)^{\mathrm{T}}\left(\mathrm{a}_2-\frac{\mathrm{a}_1+\mathrm{b}_1}{2}\right) \\ &\quad + (\mathrm{b}_1-\mathrm{a}_1)^{\mathrm{T}}\left(\mathrm{b}_2-\frac{\mathrm{a}_1+\mathrm{b}_1}{2}\right), \quad (84)\\ &= d(A,B)^2 + \frac{1}{2}\underbrace{(\mathrm{a}_1-\mathrm{b}_1)^{\mathrm{T}}(\mathrm{a}_2-\mathrm{a}_1)}_{\geq 0, \text{ by Theorem 2}} \\ &\quad + \frac{1}{2}\underbrace{(\mathrm{b}_1-\mathrm{a}_1)^{\mathrm{T}}(\mathrm{b}_2-\mathrm{b}_1)}_{\geq 0, \text{ by Theorem 2}}, \quad (85)\\ &\geq d(A,B)^2. \quad (86)\end{aligned}$$

where the inequality follows from Theorem 2 since $\|\mathrm{a}_1 - \mathrm{b}_1\| = d(A,B) = d(\mathrm{a}_1, B) = d(A, \mathrm{b}_1)$. Moreover, it follows from the Cauchy-Schwartz inequality that

$$(\mathrm{a}_1-\mathrm{b}_1)^{\mathrm{T}}(\mathrm{a}_2-\mathrm{b}_2) \leq \|\mathrm{a}_1-\mathrm{b}_1\|\|\mathrm{a}_2-\mathrm{b}_2\| = d(A,B)^2. \quad (87)$$

Hence, since $(\mathrm{a}_1-\mathrm{b}_1)^{\mathrm{T}}(\mathrm{a}_2-\mathrm{b}_2) = \|\mathrm{a}_1-\mathrm{b}_1\|^2 = \|\mathrm{a}_2-\mathrm{b}_2\|^2$, one always has

$$\mathrm{a}_1 - \mathrm{b}_1 = \mathrm{a}_2 - \mathrm{b}_2. \quad (88)$$

Also observe from (85) that

$$(\mathrm{a}_1 - \mathrm{b}_1)^{\mathrm{T}}(\mathrm{a}_1 - \mathrm{a}_2) = 0, \quad (89a)$$
$$(\mathrm{a}_1 - \mathrm{b}_1)^{\mathrm{T}}(\mathrm{b}_1 - \mathrm{b}_2) = 0. \quad (89b)$$

Therefore, the result can be verified as follows:

$$\begin{aligned}(\mathrm{a}_2-\mathrm{b}_2)^{\mathrm{T}}\left(\mathrm{x}-\frac{\mathrm{a}_2+\mathrm{b}_2}{2}\right) &= (\mathrm{a}_1-\mathrm{b}_1)^{\mathrm{T}}\left(\mathrm{x}-\frac{\mathrm{a}_2+\mathrm{b}_2}{2}\right), \quad (90)\\ &= (\mathrm{a}_1-\mathrm{b}_1)^{\mathrm{T}}\left(\mathrm{x}-\frac{\mathrm{a}_1+\mathrm{b}_1}{2}\right) \\ &\quad + \underbrace{(\mathrm{a}_1-\mathrm{b}_1)^{\mathrm{T}}\left(\frac{\mathrm{a}_1+\mathrm{b}_1}{2}-\frac{\mathrm{a}_2+\mathrm{b}_2}{2}\right)}_{=0, \text{ by (89)}}, \quad (91)\\ &= (\mathrm{a}_1-\mathrm{b}_1)^{\mathrm{T}}\left(\mathrm{x}-\frac{\mathrm{a}_1+\mathrm{b}_1}{2}\right). \quad (92)\end{aligned}$$

■

## Appendix E
## On the Jacobian of Metric Projection

A well known property of metric projections is being nonexpansive:

**Lemma 5.** Webster (1995). *The metric projection onto a closed convex set $A \subseteq \mathbb{R}^n$ is Lipschitz continuous with Lipschitz constant 1, i.e. $\|\Pi_A(\mathrm{x}) - \Pi_A(\mathrm{y})\| \leq \|\mathrm{x}-\mathrm{y}\|$ for all $\mathrm{x}, \mathrm{y} \in \mathbb{R}^n$.*

Note that a Lipschitz function in $\mathbb{R}^n$ is differentiable almost everywhere, and $\Pi_A$ is piecewise continuously differentiable Kuntz and Scholtes (1994).

**Lemma 6.** Holmes (1973); Fitzpatrick and Phelps (1982). *The Jacobian $\mathbf{J}_{\Pi_K}(\mathrm{x})$ of the metric projection onto a closed convex set $K \subseteq \mathbb{R}^n$ with twice continuously differentiable ($\mathcal{C}^2$) boundary is a positive semi-definite and symmetric operator of norm at most unity, i.e.,*

$$\mathbf{0} \preccurlyeq \mathbf{J}_{\Pi_K}(\mathrm{x}) \preccurlyeq \mathbf{I}, \quad \forall \mathrm{x} \in \mathbb{R}^n \setminus K, \quad (93)$$

*and one has $\mathbf{J}_{\Pi_K}(\mathrm{x})(\mathrm{x} - \Pi_K(\mathrm{x})) = 0$.*

The Jacobian matrix of the metric projection onto a convex set can be analytically obtained using its functional representation in terms of a level set of a convex function:

**Lemma 7.** *Let $K \in \mathbb{R}^n$ be a closed convex set associated with a twice continuously differentiable ($\mathcal{C}^2$) convex function $f : \mathbb{R}^n \to \mathbb{R}$ such that $K = f^{-1}(-\infty, c]$ for some $c \in \mathbb{R}$; and let $\nabla f : \mathbb{R}^n \to \mathbb{R}^n$ and $\nabla^2 f : \mathbb{R}^n \to \mathbb{R}^{n\times n}$ denote the gradient and Hessian of function $f$, respectively.*

*Then, the Jacobian $\mathbf{J}_{\Pi_K}(\mathrm{x})$ of the metric projection of $\mathrm{x} \in \mathbb{R}^n \setminus K$ onto $K$ is given by*

$$\mathbf{J}_{\Pi_K}(\mathrm{x}) = \mathbf{Q}(\mathbf{I}+\mathbf{Q}\mathbf{P}\mathbf{Q})^{-1}\mathbf{Q} = \mathbf{Q} - \mathbf{I} + (\mathbf{I}+\mathbf{Q}\mathbf{P}\mathbf{Q})^{-1}, \quad (94)$$

*where*

$$\mathbf{Q} := \mathbf{I} - \frac{\big(\mathrm{x} - \Pi_K(\mathrm{x})\big)\big(\mathrm{x} - \Pi_K(\mathrm{x})\big)^{\mathrm{T}}}{\|\mathrm{x} - \Pi_K(\mathrm{x})\|^2}, \quad (95)$$

$$\mathbf{P} := \frac{\|\mathrm{x} - \Pi_K(\mathrm{x})\|}{\|\nabla f(\Pi_K(\mathrm{x}))\|}\nabla^2 f(\Pi_K(\mathrm{x})). \quad (96)$$

**Proof.** Using the relation between $K$ and $f$, one can rewrite the metric project onto $K$ as

$$\Pi_K(\mathrm{x}) = \underset{\mathrm{y}\in K}{\arg\min}\ \|\mathrm{y}-\mathrm{x}\| = \underset{f(\mathrm{y})\leq c}{\arg\min}\ \|\mathrm{y}-\mathrm{x}\|. \quad (97)$$

Further, due to the optimality of $\Pi_K(\mathrm{x})$, the outward surface normal of $K$ at $\Pi_K(\mathrm{x})$ is given by $\frac{\mathrm{x}-\Pi_K(\mathrm{x})}{\|\mathrm{x}-\Pi_K(\mathrm{x})\|} = \frac{\nabla f(\Pi_K(\mathrm{x}))}{\|\nabla f(\Pi_K(\mathrm{x}))\|}$, and we have

$$\mathrm{x} = \Pi_K(\mathrm{x}) + \|\mathrm{x}-\Pi_K(\mathrm{x})\|\frac{\nabla f(\Pi_K(\mathrm{x}))}{\|\nabla f(\Pi_K(\mathrm{x}))\|}. \quad (98)$$

Hence, using $\mathbf{J}_{\Pi_K}(\mathrm{x})(\mathrm{x}-\Pi_K(\mathrm{x})) = 0$ (Lemma 6), the derivative of (98) yields

$$\mathbf{J}_{\Pi_K}(\mathrm{x}) = (\mathbf{I}-\mathbf{QP})^{-1}\mathbf{Q}. \quad (99)$$

Note that it is not straightforward to observe that the closed form of $\mathbf{J}_{\Pi_K}(\mathrm{x})$ in (99) is positive definite and symmetric (Lemma 6). Alternatively, using the matrix identity $(\mathbf{I}+\mathbf{AB})^{-1}\mathbf{A} = \mathbf{A}(\mathbf{I}+\mathbf{BA})^{-1}$ Petersen and Pedersen (2012) and $\mathbf{QQ} = \mathbf{Q}$, a more informative closed form of $\mathbf{J}_{\Pi_K}(\mathrm{x})$ can be obtained as follows:

$$\mathbf{J}_{\Pi_K}(\mathrm{x}) = (\mathbf{I}-\mathbf{QP})^{-1}\mathbf{Q} = \underbrace{(\mathbf{I}-\mathbf{QQP})^{-1}\mathbf{Q}}_{=\mathbf{Q}(\mathbf{I}-\mathbf{QPQ})^{-1}}\mathbf{Q}, \quad (100)$$

$$= \mathbf{Q}(\mathbf{I}-\mathbf{QPQ})^{-1}\mathbf{Q}. \quad (101)$$

Moreover, using a special case of Woodbury matrix identity (a.k.a. the matrix inversion lemma) Petersen and Pedersen (2012),

$$(\mathbf{I}+\mathbf{QP})^{-1} = \mathbf{I}-\mathbf{Q}(\mathbf{I}+\mathbf{PQ})^{-1}\mathbf{P}, \quad (102)$$

we also have

$$\mathbf{J}_{\Pi_K}(\mathrm{x}) = (\mathbf{I}-\mathbf{QP})^{-1}\mathbf{Q} = \big(\mathbf{I}-\mathbf{Q}(\mathbf{I}+\mathbf{PQ})^{-1}\mathbf{P}\big)\mathbf{Q}, \quad (103)$$

$$= \mathbf{Q}-\mathbf{I}+\underbrace{\mathbf{I}-\mathbf{Q}(\mathbf{I}+\mathbf{PQQ})^{-1}\mathbf{PQ}}_{=(\mathbf{I}+\mathbf{QPQ})^{-1}}, \quad (104)$$

$$= \mathbf{Q}-\mathbf{I}+(\mathbf{I}+\mathbf{QPQ})^{-1}. \quad (105)$$

Recall that $\mathbf{QQ} = \mathbf{Q}$. Thus, the lemma follows. ■

**Lemma 8.** *Let $K_1, K_2 \in \mathbb{R}^n$ be two closed convex sets associated with twice differentiable convex functions $f_1 : \mathbb{R}^n \to \mathbb{R}$ and $f_2 : \mathbb{R}^n \to \mathbb{R}$, respectively, such that $K_1 = f_1^{-1}(-\infty, c_1]$ and $K_2 = f_2^{-1}(-\infty, c_2]$ for some $c_1, c_2 \in \mathbb{R}$. And let $\mathrm{x} \in \mathbb{R}^n \setminus (K_1 \cup K_2)$ with $\Pi_{K_1}(\mathrm{x}) = \Pi_{K_2}(\mathrm{x})$.*

*Then the following equivalence holds*

$$\frac{\nabla^2 f_1(\Pi_{K_1}(\mathrm{x}))}{\|\nabla f_1(\Pi_{K_1}(\mathrm{x}))\|} \preccurlyeq \frac{\nabla^2 f_2(\Pi_{K_2}(\mathrm{x}))}{\|\nabla f_2(\Pi_{K_2}(\mathrm{x}))\|} \iff \mathbf{J}_{\Pi_{K_1}}(\mathrm{x}) \succcurlyeq \mathbf{J}_{\Pi_{K_2}}(\mathrm{x}). \quad (106)$$

**Proof.** The result directly follows from Lemma 7 and the following matrix relation of positive definite matrices, $\mathbf{A}$ and $\mathbf{B}$, Bhatia (2007)

$$\mathbf{A} \preccurlyeq \mathbf{B} \iff \mathbf{A}^{-1} \succcurlyeq \mathbf{B}^{-1}.$$ ■

**Lemma 9.** *Let $K_1, K_2 \subseteq \mathbb{R}^n$ be two convex sets with twice continuously differentiable ($\mathcal{C}^2$) boundary.*

*If $K_1 \supseteq K_2$, then the Jacobians $\mathbf{J}_{\Pi_{K_1}}(\mathrm{x})$ and $\mathbf{J}_{\Pi_{K_2}}(\mathrm{x})$ of metric projections onto $K_1$ and $K_2$, respectively, satisfy*

$$\mathbf{J}_{\Pi_{K_1}}(\mathrm{x}) \succcurlyeq \mathbf{J}_{\Pi_{K_2}}(\mathrm{x}), \quad (107)$$

*for all $\mathrm{x} \in \mathbb{R}^n \setminus K_1$ with $\Pi_{K_1}(\mathrm{x}) = \Pi_{K_2}(\mathrm{x})$.*

**Proof.** For any $\mathrm{x} \in \mathbb{R}^n \setminus K_1$ with $\Pi_{K_1}(\mathrm{x}) = \Pi_{K_2}(\mathrm{x})$ and $\mathrm{y} \in \mathbb{R}^n$, one can write the metric projection of $\mathrm{x}+\mathrm{y}$ onto $K_1$ and $K_2$, respectively, as

$$\Pi_{K_1}(\mathrm{x}+\mathrm{y}) = \Pi_{K_1}(\mathrm{x}) + \mathbf{J}_{\Pi_{K_1}}(\mathrm{x})\mathrm{y} + o(\mathrm{y}), \quad (108a)$$

$$\Pi_{K_2}(\mathrm{x}+\mathrm{y}) = \Pi_{K_2}(\mathrm{x}) + \mathbf{J}_{\Pi_{K_2}}(\mathrm{x})\mathrm{y} + o(\mathrm{y}), \quad (108b)$$

where $\lim_{\|\mathrm{y}\|\to 0}\frac{o(\mathrm{y})}{\|\mathrm{y}\|} = 0$. Further, since $K_1 \supseteq K_2$, by the monotonicity of metric projections, we have

$$\|\mathrm{x}+\mathrm{y}-\Pi_{K_1}(\mathrm{x}+\mathrm{y})\|^2 \leq \|\mathrm{x}+\mathrm{y}-\Pi_{K_2}(\mathrm{x}+\mathrm{y})\|^2. \quad (109)$$

Now it follows from (108), (109) and Lemma 6 that

$$\frac{\big\|\big(I-\mathbf{J}_{\Pi_{K_2}}(\mathrm{x})\big)\mathrm{y}\big\|^2}{\|\mathrm{y}\|^2} - \frac{\big\|\big(I-\mathbf{J}_{\Pi_{K_1}}(\mathrm{x})\big)\mathrm{y}\big\|^2}{\|\mathrm{y}\|^2} \geq \frac{\|\mathrm{x}-\Pi_{K_1}(\mathrm{x})-o(\mathrm{y})\|^2}{\|\mathrm{y}\|^2} - \frac{\|\mathrm{x}-\Pi_{K_2}(\mathrm{x})-o(\mathrm{y})\|^2}{\|\mathrm{y}\|^2} + \frac{2\mathrm{y}^{\mathrm{T}}\big(\mathbf{J}_{\Pi_{K_1}}(\mathrm{x})-\mathbf{J}_{\Pi_{K_1}}(\mathrm{x})\big)o(\mathrm{y})}{\|\mathrm{y}\|^2}, \quad (110)$$

where the right hand side converges to zero as $\|\mathrm{y}\| \to 0$. Therefore, for any $\mathrm{y} \in \mathbb{R}^n$, one always has

$$\big\|\big(I-\mathbf{J}_{\Pi_{K_2}}(\mathrm{x})\big)\mathrm{y}\big\|^2 \geq \big\|\big(I-\mathbf{J}_{\Pi_{K_1}}(\mathrm{x})\big)\mathrm{y}\big\|^2. \quad (111)$$

Thus, the result follows since $\mathbf{0} \preccurlyeq \mathbf{J}_{\Pi_{K_1}}(\mathrm{x}), \mathbf{J}_{\Pi_{K_2}}(\mathrm{x}) \preccurlyeq \mathbf{I}$ (Lemma 6). ■

## Appendix F
## On the Computation of Metric Projection onto Convex Polytopes

One can recast metric projection onto convex polytopes and distance between them as convex quadratic optimization problems, and solve them iteratively using the active set method, summarized below.

Consider a convex quadratic optimization problem with equality and inequality constraints (QP-IE):

$$\begin{aligned} \min_{\mathrm{x}\in\mathbb{R}^n} \ & f(\mathrm{x}) = \frac{1}{2}\mathrm{x}^{\mathrm{T}}\mathbf{Q}\,\mathrm{x} + \mathrm{x}^{\mathrm{T}}\mathrm{c} \\ \text{subject to } & \mathrm{a}_i^{\mathrm{T}}\mathrm{x} = b_i, \ i \in \mathcal{E}, \\ & \mathrm{a}_j^{\mathrm{T}}\mathrm{x} \geq b_j, \ j \in \mathcal{I}, \end{aligned} \qquad \text{(QP-IE)}$$

where $\mathbf{Q} \in \mathbb{R}^{n\times n}$ is a positive definite matrix, $\mathcal{E}$ and $\mathcal{I}$ are sets of indices for equality and inequality constraints, respectively, and $\mathrm{c}, \mathrm{a}_i \in \mathbb{R}^n$ and $b_i \in \mathbb{R}$, where $i \in \mathcal{E} \cup \mathcal{I}$. Also, let

$$\mathcal{X} := \left\{ \mathrm{x}\in\mathbb{R}^n \middle| \mathrm{a}_i{}^{\mathrm{T}}\mathrm{x} = b_i \ \forall i\in\mathcal{E}, \ \mathrm{a}_j{}^{\mathrm{T}}\mathrm{x} \geq b_j \ \forall j\in\mathcal{I} \right\} \quad (112)$$

denote the set of feasible solutions of (QP-IE), and let $\mathcal{A}(\mathrm{x}) := \mathcal{E} \cup \left\{ j \in \mathcal{I} | \, \mathrm{a}_i{}^{\mathrm{T}}\mathrm{x} = b_j \right\}$ be the index set of active constraints at a feasible solution $\mathrm{x} \in \mathcal{X}$.

Among many alternative solvers Wright and Nocedal (1999); Boyd and Vandenberghe (2004), active set methods offers an iterative solution for the convex quadratic optimization problem (QP-IE), whose iterations, denoted by $\mathrm{x}_{k+1} = \mathtt{AS}(\mathrm{x}_k)$, satisfy for any feasible solution $\mathrm{x}_k \in \mathcal{X}$ the properties:

(i) (Feasible Iterations) $\mathtt{AS}(\mathrm{x}_k) \in X$,

(ii) (Monotonic Decrease) $f(\mathrm{x}_k) \geq f(\mathtt{AS}(\mathrm{x}_k))$,

(iii) (Finite-Step Global Convergence) $\mathtt{AS}(\mathrm{x}_k)$ converges in polynomial steps to the global solution of (QP-IE).

More precisely, to find the global solution of (QP-IE), the active set method starts with a feasible solution $\mathrm{x}_0 \in \mathcal{X}$ and, at each iteration $k \in \mathbb{N}$, it solves an associated convex quadratic optimization problem with equality constraint to find an update step, $\mathrm{p}_k \in \mathbb{R}^n$:

$$\begin{aligned} \min_{\mathrm{p}_k\in\mathbb{R}^n} \ & \frac{1}{2}\mathrm{p}_k{}^{\mathrm{T}}\mathbf{Q}\,\mathrm{p}_k + \mathrm{p}_k^{\mathrm{T}}\mathrm{g}_k \\ \text{subject to } & \mathrm{a}_i^{\mathrm{T}}\mathrm{p}_k = 0, \ i \in \mathcal{W}_k \end{aligned} \qquad \text{(QP-EQ)}$$

where $\mathrm{g}_k = \mathbf{Q}\mathrm{x}_k + \mathrm{c}$ and $\mathcal{W}_k \subseteq \mathcal{A}(\mathrm{x}_k)$ is a subset of the indices of the active constraints at $\mathrm{x}_k$ with linearly independent constraint gradients, $\mathrm{a}_i$'s, and is referred to as the *working set*. The solution to (QP-EQ), denoted by $(\mathrm{p}_k, \lambda_k) = \mathtt{SolveQPEQ}(\mathrm{x}_k, \mathcal{W}_k)$, can be found by solving

$$\begin{bmatrix} \mathbf{Q} & \mathbf{A}^{\mathrm{T}} \\ \mathbf{A} & \mathbf{0} \end{bmatrix} \begin{bmatrix} -\mathrm{p}_k \\ \lambda_k \end{bmatrix} = \begin{bmatrix} \mathrm{g}_k \\ 0 \end{bmatrix}, \quad (113)$$

where $\mathbf{A} = [\mathrm{a}_i{}^{\mathrm{T}}]_{i\in\mathcal{W}(\mathrm{x}_k)}$ is the Jacobian of working set constraints, and $\lambda_k$ denotes the vector of Lagrange multipliers for (QP-EQ) and is used to check the Karush-Kuhn-Tucker (KKT) optimality condition of $\mathrm{x}_k$ for (QP-IE).

**Algorithm 1:** The Active Set Algorithm Wright and Nocedal (1999)[Chapter 16]

**Input:** $\mathrm{x}_0 \in \mathcal{X}$ – Initial Feasible Solution
$\mathcal{W}_0 \subset \mathcal{A}(\mathrm{x}_0)$ – Initial Working Set
**Output:** $\mathrm{x}^* \in \mathcal{X}$ – The global solution of (QP-IE)

**for** $k = 0, 1, \ldots$ **do**
  $(\mathrm{p}_k, \lambda) \leftarrow \mathtt{SolveQPEQ}(\mathrm{x}_k, \mathcal{W}_k)$;
  **if** $\mathrm{p}_k = 0$ **then**
    **if** $\lambda_i \geq 0 \ \forall i \in \mathcal{W}_k \cap \mathcal{I}$ **then**
      $\mathrm{x}^* \leftarrow \mathrm{x}_k$; **return** $\mathrm{x}^*$;
    **else**
      $j \leftarrow \arg\min_{j\in\mathcal{W}_k\cap\mathcal{I}} \lambda_j$;
      $\mathrm{x}_{k+1} \leftarrow \mathrm{x}_k$; $\mathcal{W}_{k+1} \leftarrow \mathcal{W}_k \setminus \{j\}$;
  **else**
    $\alpha_k \leftarrow \min\left(1, \min_{i\in\mathcal{I}\setminus\mathcal{W}_k, \, \mathrm{a}_i^{\mathrm{T}}\mathrm{p}_k<0} \frac{b_i - \mathrm{a}_i^{\mathrm{T}}\mathrm{x}_k}{\mathrm{a}_i^{\mathrm{T}}\mathrm{p}_k}\right)$;
    $\mathrm{x}_{k+1} \leftarrow \mathrm{x}_k + \alpha_k \mathrm{p}_k$;
    **if** $\exists i \in \mathcal{A}(\mathrm{x}_{k+1}) \setminus \mathcal{W}_k$ **then**[18]
      $\mathcal{W}_{k+1} \leftarrow \mathcal{W}_k \cup \{i\}$;
    **else** $\mathcal{W}_{k+1} \leftarrow \mathcal{W}_k$ ;

In summary, the active set method repeatedly uses the solution of (QP-EQ) to generate a new estimated solution $\mathrm{x}_{k+1}$ for (QP-IE), and terminates at the global solution of (QP-EQ), as shown in Algorithm 1. For more details, refer to Wright and Nocedal (1999)[Chapter 16].

To conclude this part, we emphasize a virtue of the active set method beyond its polynomial time complexity. We believe its feasible iterations and guaranteed monotonic decrease make it a compelling option for general incremental anytime computations of distance between convex bodies, metric projection onto convex sets, and, of course, our "move-to-projected-goal" law in (11). This anytime nature affords opportunistic interruption of its computation while relying on the last iterated feasible solution as an estimate of the global optimal solution. In the context of dynamically evolving motion planning or dynamic settings, these interruptions can be event based and the results of the previous computation can improve the initiation of its successor.

## Appendix G
## Convexity in Polar Coordinates

Similar to the notion of convexity in Cartesian coordinates, a polar curve $\rho : (\theta_l, \theta_u) \to \mathbb{R}_{\geq 0}$ is said to be *convex* with respect to the pole if and only if its epigraph,[19] $\mathrm{epi}\rho := \left\{ (\theta, \varrho) \middle| \theta \in (\theta_l, \theta_u), \varrho \geq \rho(\theta) \right\}$, is a convex set; and, likewise, $\rho$ is said to be *concave* if and only if

its hypograph, $\mathrm{hyp}\rho := \{(\theta,\varrho)\big|\theta\in(\theta_l,\theta_u), 0\le\varrho\le\rho(\theta)\}$ is a convex set McMahon and Snyder (1898); Eggleston (1958), see Fig. 10.

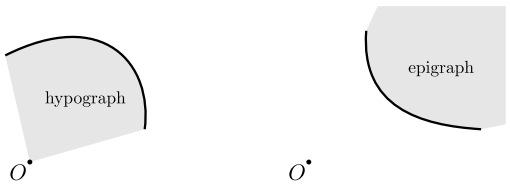


**Fig. 10.** Convexity in polar coordinates. A polar curve is convex (concave) with respect to the pole iff its epigraph (hypograph) is a convex set, as illustrated on the right (left, respectively).

Alternatively, like the first- and second-order conditions for convexity of Cartesian functions, one can verify the convexity of a polar curve as follows:

**Theorem 5.** Second-Order Convexity Condition McMahon and Snyder (1898). *A twice differentiable polar curve $\rho:(\theta_l,\theta_u)\to\mathbb{R}_{>0}$ is said to be convex with respect to the pole if* [20]

$$\Gamma := \rho^2 + 2\left(\frac{\mathrm{d}\rho}{\mathrm{d}\theta}\right)^2 - \rho\frac{\mathrm{d}^2\rho}{\mathrm{d}\theta^2} \le 0. \tag{114}$$

**Theorem 6.** Three-Point Convexity Condition Eggleston (1958). *A polar curve $\rho:(\theta_l,\theta_u)\to\mathbb{R}_{>0}$ is convex with respect to the pole if* [21]

$$\det\left(\begin{bmatrix}\frac{1}{\rho(\theta_1)} & \cos\theta_1 & \sin\theta_1\\ \frac{1}{\rho(\theta_2)} & \cos\theta_2 & \sin\theta_2\\ \frac{1}{\rho(\theta_3)} & \cos\theta_3 & \sin\theta_3\end{bmatrix}\right)\cdot\det\left(\begin{bmatrix}1 & \cos\theta_1 & \sin\theta_1\\ 1 & \cos\theta_2 & \sin\theta_2\\ 1 & \cos\theta_3 & \sin\theta_3\end{bmatrix}\right)\le 0, \tag{115}$$

*for all $\theta_1,\theta_2,\theta_3\in(\theta_l,\theta_u)$.*

Note that the second determinant term in (115) quantifies the circular order of $\theta_1$, $\theta_2$ and $\theta_3$, i.e., it is positive (negative) if these angles are given in counter-clockwise (clockwise, respectively) order.

In accordance with Theorem 6, since a LIDAR scanner has a fixed angular resolution in practice, say $\Delta\theta\in(0,\pi)$, to check the convexity of a LIDAR scan in counter-clockwise angular order, we find it convenient to define

$$\Upsilon(\theta) := \det\left(\begin{bmatrix}\frac{1}{\rho(\theta-\Delta\theta)} & \cos(\theta-\Delta\theta) & \sin(\theta+\Delta\theta)\\ \frac{1}{\rho(\theta)} & \cos(\theta) & \sin(\theta)\\ \frac{1}{\rho(\theta+\Delta\theta)} & \cos(\theta+\Delta\theta) & \sin(\theta+\Delta\theta)\end{bmatrix}\right). \tag{116}$$

Therefore one can identify the convex polar curve segments of a LIDAR scan using the convexity measures $\Gamma$ (114) and $\Upsilon$ (116) as illustrated in Fig. 11.

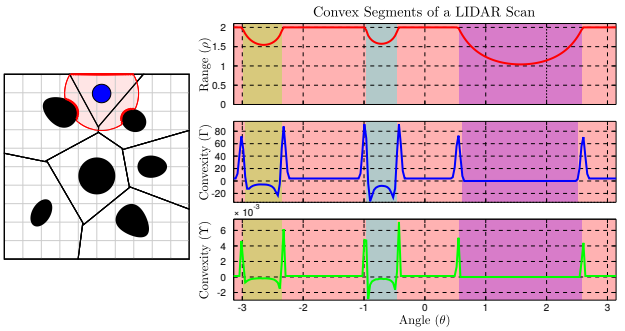


**Fig. 11.** Segmentation of a LIDAR scan into convex polar curves using convexity measures $\Gamma$ (114) and $\Upsilon$ (115). [22] [23]

## Appendix H
## An Extension for a Discrete-Time Robot Model

Keeping in mind its potential application to online robot navigation in a nonconvex environment when combined with a standard (e.g., sampling based) motion planning algorithm — a future research direction we will explore in a subsequent paper, we now introduce a discrete-time version of the "move-to-projected-goal" law in (11) to iteratively navigate towards a designated goal location $\mathrm{x}^*\in\mathcal{F}$ as follows: for any $\mathrm{x}^k\in\mathcal{F}$,

$$\mathrm{x}^{k+1} = \mathrm{x}^k - \big(\mathrm{x}^k - \Pi_{\mathcal{LF}(\mathrm{x}^k)}(\mathrm{x}^*)\big)\Delta t, \tag{117}$$

where $k\in\mathbb{N}$ is a discrete time index, $\Delta t\in(0,1]$ is a fixed sample time (step size), and $\Pi_{\mathcal{LF}(\mathrm{x}^k)}(\mathrm{x}^*)$ (5) is the metric projection of the goal $\mathrm{x}^*$ onto the robot's local free space $\mathcal{LF}(\mathrm{x}^k)$ (10). Note that we here avoid collisions along the line segment joining consecutive robot states, $\mathrm{x}^k$ and $\mathrm{x}^{k+1}$, by limiting the range of values of $\Delta t$ to $(0,1]$ since $\mathrm{x}^{k+1}$ becomes a convex combination of the robot state $\mathrm{x}^k$ and the projected goal $\Pi_{\mathcal{LF}(\mathrm{x}^k)}(\mathrm{x}^*)$, i.e., $\mathrm{x}^{k+1} = (1-\Delta t)\mathrm{x} + \Delta t\,\Pi_{\mathcal{LF}(\mathrm{x}^k)}(\mathrm{x}^*)$, and the line segment joining them is always free of collisions (Corollary 1).

Therefore, using the continuity of the move-to-projected-goal law in (11) (Proposition 2) and the type of its stationary points (Proposition 6), one can conclude that:

**Corollary 4.** *If Assumption 2 holds for the goal and for all obstacles, then the discrete-time "move-to-projected-goal" law in (117) starting from almost any robot location in $\mathcal{F}$ (1) iteratively reaches a small neighborhood, $B(\mathrm{x}^*,\epsilon)$ for some $\epsilon>0$, of the goal $\mathrm{x}^*$ in finite steps with the guarantee of no collisions along the line segments joining two consecutive robot states, while strictly decreasing the Euclidean distance to the goal.*

Note that the discrete-time "move-to-projected-goal" law in (117) can be simply adapted to limited range sensing models, by using the robot's sensed local free space $\mathcal{LF}_{\mathcal{S}}$

(25) or the line-of-sight local free space $\mathcal{LF}_{\mathcal{L}}$ (31), as well as to the differential drive model while retaining the convergence and collision avoidance guarantees.

To demonstrate its motion pattern, we present in Fig. 12 the resulting navigation paths of the discrete-time "move-to-projected-goal" law in (117) for different sampling times and sensing models.

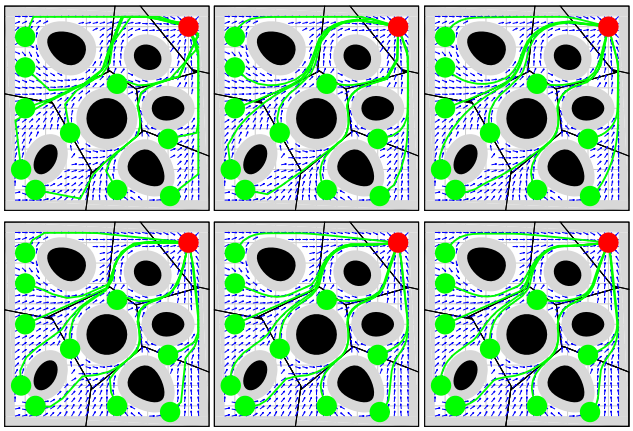

**Fig. 12.** Example navigation paths of the discrete-time "move-to-projected-goal" law for different sampling times and sensing models: (left) $\Delta t = 1$, (middle) $\Delta t = 0.5$, and (right) $\Delta t = 0.25$; and (top) local Voronoi-adjacent[3] obstacle sensing, and (bottom) a fixed radius sensory footprint.

## Appendix I
## Motion Pattern Far Away from the Goal

In Fig. 13, we present the motion pattern generated by the "move-to-projected-goal" law starting at a set of initial robot configurations far away from the goal, located at the upper right corner of a $50 \times 10$ environment populated with convex obstacles, for different sensing and actuation models.

### Funding

This work was supported in part by AFOSR CHASE MURI FA9550-10-1-0567 and in part by AFRL FA865015D1845 (subcontract 669737-1).

### Declaration of conflicting interests

The authors declare that there is no conflict of interest.

### Notes

1. Topological reasoning precludes the possibility of any continuous reactive planner achieving global asymptotic stability (i.e., guaranteeing convergence to a point goal from all initial conditions) except on a contractible space Bhatia and Szegö (2002) (e.g., absent any obstacles in the present setting). Even for deliberative navigation (i.e., when motions connecting specified initial and final desired configurations can be planned offline with perfect knowledge of the environment) it is known that non-contractible spaces do not admit continuous motion planners Farber (2003). Since, as in our problem, the free space of a robotic system is generally non-contractible, the domain of a continuous navigation planner must generally exclude at least a set of measure zero.
2. We adopt standard usage to denote by this term the use of the negative gradient field of a scalar valued function as the force or velocity control law for a fully actuated, kinematic (first-order dynamics) robot.
3. A pair of Voronoi cells in $\mathbb{R}^n$ is said to be *adjacent* if they share a $n-1$ dimensional face.
4. $\mathbb{N}$ is the set of all natural numbers; $\mathbb{R}$ and $\mathbb{R}_{>0}$ ($\mathbb{R}_{\geq 0}$) denote the set of real and positive (nonnegative) real numbers, respectively.
5. Note that $\mathcal{F} \subsetneq \mathcal{W} \setminus \bigcup_{i=1}^{m} O_i$ for a disk-shaped robot of radius $r > 0$.
6. One can generalize the same result in (9) for any $\mathrm{x} \in \mathcal{W}$ if the robot's local workspace $\mathcal{LW}(\mathrm{x})$ is defined to be
$$\mathrm{cl}\left(\left\{\mathrm{q}\in\mathcal{W}\,\middle|\,\left\|\mathrm{q}-\mathrm{x}+r\frac{\mathrm{x}-\Pi_{\overline{O}_i}(\mathrm{x})}{\left\|\mathrm{x}-\Pi_{\overline{O}_i}(\mathrm{x})\right\|}\right\| < \left\|\mathrm{q}-\Pi_{\overline{O}_i}(\mathrm{x})\right\|, \forall i\right\}\right),$$
which is empty whenever $\mathrm{x} \in O_i$ for some $i = 1, \ldots, m$; otherwise, is equal to (8). Here, $\mathrm{cl}(A)$ denotes the closure of a set $A$.
7. The erosion of a closed half-space by an open ball is a closed half-space. Hence, since the erosion operation is distributed over set intersection Haralick et al. (1987), and a closed convex set can be defined as (possibly infinite) intersection of closed half-spaces Boyd and Vandenberghe (2004), and an arbitrary intersection of closed sets is closed Munkres (2000), the erosion of a closed convex set by an open ball is a closed convex set.
8. For any two symmetric matrices $\mathbf{A}, \mathbf{B} \in \mathbb{R}^{N\times N}$, $\mathbf{A} \prec \mathbf{B}$ (and $\mathbf{A} \preccurlyeq \mathbf{B}$) means that $\mathbf{B} - \mathbf{A}$ is positive definite (positive semidefinite, respectively).
9. Here, we require the goal to be in the interior $\mathring{\mathcal{F}}$ of $\mathcal{F}$ to guarantee that the differential-drive robot can nearly align its orientation with the (local) goal in finite time.
10. In the design of angular motion we particularly select a local target location, $\frac{\Pi_{\mathcal{L}\mathcal{F}_\omega(\mathrm{x})}(\mathrm{x}^*)+\Pi_{\mathcal{LF}(\mathrm{x})}(\mathrm{x}^*)}{2} \in \mathring{\mathcal{F}}$ given $\mathrm{x}^* \in \mathring{\mathcal{F}}$, in the interior $\mathring{\mathcal{F}}$ of $\mathcal{F}$ to increase the convergence rate of the resulting vector field. One can consider other convex combinations of $\Pi_{\mathcal{L}\mathcal{F}_\omega(\mathrm{x})}(\mathrm{x}^*)$ and $\Pi_{\mathcal{LF}(\mathrm{x})}(\mathrm{x}^*)$ (or an eroded version of $\mathcal{LF}$ by a certain clearance margin), and the resulting vector field retains qualitative properties.
11. In (40), one can limit a differential drive robot to move only in forward direction by restricting the linear velocity input to nonnegative reals and using $\mathrm{atan2}$ instead of $\mathrm{atan}$ while computing the angular velocity input.

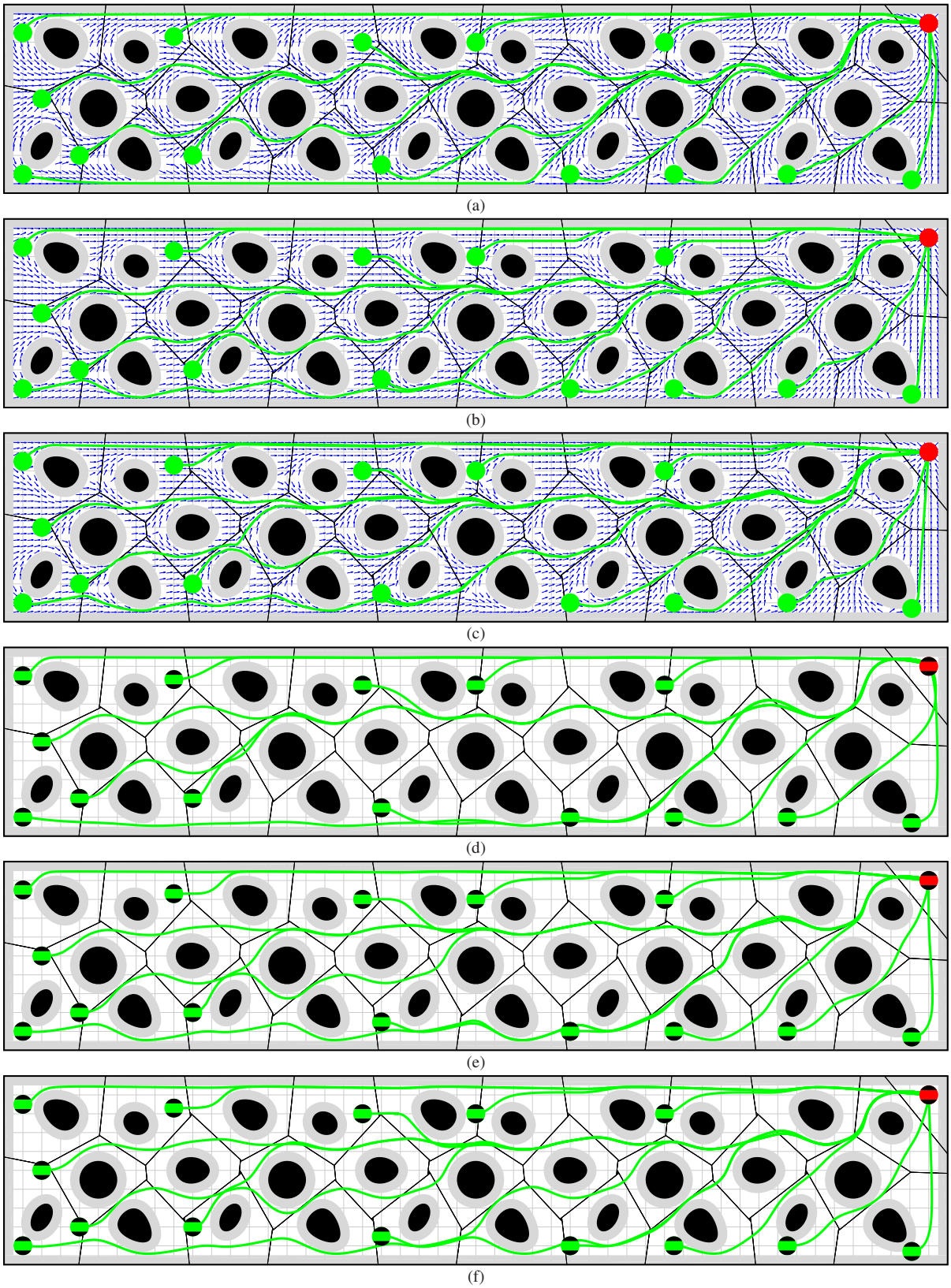


**Fig. 13.** Example navigation trajectories of the "move-to-projected-goal" law starting at a set of initial conditions (green) far away from the goal (red) for different sensing and actuation models: (a,b,c) a fully actuated robot, (d,e,f) a differential drive robot, (a,d) local Voronoi-adjacent[3] obstacle sensing, (b,e) a fixed radius sensory footprint, (c,f) a limited range line-of-sight sensor.

12. For all simulations we set $r = 0.5$, $R = 2$ and $k = 1$, and all simulations are obtained through numerical integration of the associated "move-to-projected-goal" law using the `ode45` function of MATLAB.
13. http://www.turtlebot.com/
14. http://www.hokuyo-aut.jp/
15. http://www.vicon.com/
16. http://www.python.org/
17. http://www.ros.org/
18. The working set $\mathcal{W}_k$ should always contain the indices of linearly independent constraint gradients and so should be updated accordingly.
19. Note that here the epigraph and the hypograph of a polar curve are given in polar coordinates, and one can equivalently write them in Cartesian coordinates as

$$\mathrm{epi}\rho = \big\{(\varrho\cos\theta, \varrho\sin\theta)\big|\theta \in (\theta_l, \theta_u), \varrho \geq \rho(\theta)\big\},$$
$$\mathrm{hyp}\rho = \big\{(\varrho\cos\theta, \varrho\sin\theta)\big|\theta \in (\theta_l, \theta_u), 0 \leq \varrho \leq \rho(\theta)\big\}.$$

20. In McMahon and Snyder (1898), the convexity of a polar curve with respect to the pole is characterized based on its tangent lines: a polar curve at a point is convex iff the curve in a small neighborhood of that point lies on the opposite side of the tangent at that point to the pole. Accordingly, the second-order convexity condition in (114) is derived using the perpendicular distance $p$ of the pole to the tangent line of a polar curve $\rho$ at point $(\theta, \rho(\theta))$, given by

$$\frac{1}{p^2} = u^2 + \left(\frac{\mathrm{d}u}{\mathrm{d}\theta}\right)^2,$$

where $u := \frac{1}{\rho}$; and the polar curve $\rho$ is said to be convex with respect to the pole if and only if $\frac{\mathrm{d}p}{\mathrm{d}\rho}$ is negative, where

$$\frac{\mathrm{d}p}{\mathrm{d}\rho} = p^3u^2\left(u + \frac{\mathrm{d}^2u}{\mathrm{d}\theta^2}\right) = \frac{p^3}{\rho^2}\left(\rho^2 + 2\left(\frac{\mathrm{d}\rho}{\mathrm{d}\theta}\right)^2 - \rho\frac{\mathrm{d}^2\rho}{\mathrm{d}\theta^2}\right).$$

21. Let $\mathrm{v}_t = (\cos\theta_t, \sin\theta_t)$ and $\mathrm{p}_t = (\rho(\theta_t)\cos\theta_t, \rho(\theta_t)\sin\theta_t)$ for $t = 1, 2, 3$. Then, to have a geometric understanding of the three-point convexity condition one can equivalently rewrite (115) as

$$\big((\mathrm{p}_2 - \mathrm{p}_1)\times(\mathrm{p}_3 - \mathrm{p}_2)\big)\cdot\big((\mathrm{v}_2 - \mathrm{v}_1)\times(\mathrm{v}_3 - \mathrm{v}_2)\big) \leq 0,$$

where $\times$ and $\cdot$ denote the cross and dot products, respectively.
22. Here, we set the LIDAR's angular resolution to $\Delta\theta = \frac{\pi}{100}$, and approximately compute the first- and second-order derivatives of a simulated LIDAR range data, respectively, using its three-point first- and second-order central differences Fornberg (1988) after smoothing with a five-point Gaussian moving average filter with unit variance, $\sigma^2 = 1$ Szeliski (2011).
23. A practical heuristic for identifying convex segments of a LIDAR scan is its segmentation based on local maxima; however, such a heuristic approach might detect some concave curve segments in addition to all convex segments in a LIDAR scan.

## References


Arslan O (2016) *Clustering-Based Robot Navigation and Control*. PhD Thesis, University of Pennsylvania.

Arslan O, Guralnik DP and Koditschek DE (2016) Coordinated robot navigation via hierarchical clustering. *Robotics, IEEE Transactions on* 32(2): 352–371.

Arslan O and Koditschek DE (2016a) Exact robot navigation using power diagrams. In: *IEEE International Conference on Robotics and Automation*. pp. 1–8.

Arslan O and Koditschek DE (2016b) Sensor-based reactive navigation in unknown convex sphere worlds. *The 12th International Workshop on the Algoritmic Foundations of Robotics (WAFR)* .

Arslan O and Koditschek DE (2016c) Voronoi-based coverage control of heterogeneous disk-shaped robots. In: *IEEE International Conference on Robotics and Automation*. pp. 4259–4266.

Arslan O and Koditschek DE (2017) Smooth extensions of feedback motion planners via reference governors. In: *IEEE International Conference on Robotics and Automation*. pp. 4414–4421.

Arslan O, Pacelli V and Koditschek DE (2017) Sensory steering for sampling-based motion planning. In: *IEEE/RSJ International Conference on Intelligent Robots and Systems*. pp. 3708–3715.

Astolfi A (1999) Exponential stabilization of a wheeled mobile robot via discontinuous control. *Journal of Dynamic Systems, Measurement, and Control* 121(1): 121–126.

Aurenhammer F (1987) Power diagrams: Properties, algorithms and applications. *SIAM Journal on Computing* 16(1): 78–96.

Bhatia NP and Szegö GP (2002) *Stability Theory of Dynamical Systems*, volume 161. Springer Science & Business Media.

Bhatia R (2007) *Positive Definite Matrices*. Princeton Series in Applied Mathematics. Princeton University Press.

Borenstein J and Koren Y (1991) The vector field histogram-fast obstacle avoidance for mobile robots. *IEEE Transactions on Robotics and Automation* 7(3): 278–288.

Boyd S and Vandenberghe L (2004) *Convex Optimization*. Cambridge University Press.

Brockett RW (1983) *Asymptotic stability and feedback stabilization*. Defense Technical Information Center.

Bullo F, Cortés J and Martinez S (2009) *Distributed Control of Robotic Networks: A Mathematical Approach to Motion Coordination Algorithms*. Princeton University Press.

Burridge RR, Rizzi AA and Koditschek DE (1999) Sequential composition of dynamically dexte-rous robot behaviors. *The International Journal of Robotics Research* 18(6): 535–555.

Chaney RW (1990) Piecewise $C^k$ functions in nonsmooth analysis. *Nonlinear Analysis: Theory, Methods & Applications* 15(7): 649–660.

Chazelle B (1987) Approximation and decomposition of shapes. *Algorithmic and Geometric Aspects of Robotics* 1: 145–185.

Choset H and Burdick J (2000) Sensor-based exploration: The hierarchical generalized Voronoi graph. *The International Journal of Robotics Research* 19(2): 96–125.

Choset H, Lynch KM, Hutchinson S, Kantor GA, Burgard W, Kavraki LE and Thrun S (2005) *Principles of Robot Motion: Theory, Algorithms, and Implementations*. MIT Press.

Choset H and Pignon P (1998) Coverage path planning: The boustrophedon cellular decomposition. In: *Field and Service Robotics*. Springer London, pp. 203–209.

Conner DC, Choset H and Rizzi AA (2009) Flow-through policies for hybrid controller synthesis applied to fully actuated systems. *IEEE Transactions on Robotics* 25(1): 136–146.

Conner DC, Choset H and Rizzi AA (2011) Integrating planning and control for single-bodied wheeled mobile robots. *Autonomous Robots* 30(3): 243–264.

Connolly CI and Grupen RA (1993) The applications of harmonic functions to robotics. *Journal of Robotic Systems* 10(7): 931–946.

Cortés J, Martınez S, Karatas T and Bullo F (2004) Coverage control for mobile sensing networks. *IEEE Transactions on Robotics and Automation,* 20(2): 243–255.

Eggleston HG (1958) *Convexity*. Cambridge University Press.

Farber M (2003) Topological complexity of motion planning. *Discrete and Computational Geometry* 29(2): 211–221.

Fierro R and Lewis FL (1997) Control of a nonholomic mobile robot: Backstepping kinematics into dynamics. *Journal of Robotic Systems* 14(3): 149–163.

Filippidis I and Kyriakopoulos KJ (2011) Adjustable navigation functions for unknown sphere worlds. In: *IEEE Decision and Control and European Control Conference*. pp. 4276–4281.

Filippidis IF and Kyriakopoulos KJ (2012) Navigation functions for everywhere partially sufficiently curved worlds. In: *IEEE International Conference on Robotics and Automation*. pp. 2115–2120.

Fiorini P and Shiller Z (1998) Motion planning in dynamic environments using velocity obstacles. *The International Journal of Robotics Research* 17(7): 760–772.

Fitzpatrick S and Phelps RR (1982) Differentiability of the metric projection in Hilbert space. *Transactions of the American Mathematical Society* 270(2): 483–501.

Fornberg B (1988) Generation of finite difference formulas on arbitrarily spaced grids. *Mathematics of Computation* 51(184): 699–706.

Foskey M, Garber M, Lin MC and Manocha D (2001) A Voronoi-based hybrid motion planner. In: *IEEE/RSJ International Conference on Intelligent Robots and Systems*, volume 1. pp. 55–60.

Fox D, Burgard W and Thrun S (1997) The dynamic window approach to collision avoidance. *IEEE Robotics Automation Magazine* 4(1): 23–33.

Haralick RM, Sternberg SR and Zhuang X (1987) Image analysis using mathematical morphology. *IEEE Transactions on Pattern Analysis and Machine Intelligence* 9(4): 532–550.

Henry P, Vollmer C, Ferris B and Fox D (2010) Learning to navigate through crowded environments. In: *IEEE International Conference on Robotics and Automation*. pp. 981–986.

Hirsch MW, Smale S and Devaney RL (2003) *Differential Equations, Dynamical Systems, and an Introduction to Chaos*. 2nd edition. Academic press.

Holleman C and Kavraki LE (2000) A framework for using the workspace medial axis in PRM planners. In: *IEEE International Conference on Robotics and Automation*, volume 2. pp. 1408–1413.

Holmes RB (1973) Smoothness of certain metric projections on Hilbert space. *Transactions of the American Mathematical Society* 184: 87–100.

Ilhan BD, Johnson AM and Koditschek DE (2018) Autonomous legged hill ascent. *Journal of Field Robotics* 0(0).

Johnson AM, Hale MT, Haynes GC and Koditschek DE (2011) Autonomous legged hill and stairwell ascent. In: *IEEE Int. Symp. on Safety, Security, Rescue Robotics*. pp. 134–142.

Karaman S and Frazzoli E (2012) High-speed flight in an ergodic forest. In: *IEEE International Conference on Robotics and Automation*. pp. 2899–2906.

Khalil HK (2001) *Nonlinear Systems*. 3rd edition. Prentice Hall.

Khatib O (1986) Real-time obstacle avoidance for manipulators and mobile robots. *The International Journal of Robotics Research* 5(1): 90–98.

Koditschek DE (1987a) Adaptive techniques for mechanical systems. In: *Proc. 5th. Yale Workshop on Adaptive Systems*. pp. 259–265.

Koditschek DE (1987b) Exact robot navigation by means of potential functions: Some topological considerations. In: *IEEE International Conference on Robotics and Automation*. pp. 1–6.

Koditschek DE (1991) Some applications of natural motion control. *Journal of Dynamic Systems, Measurement, and Control* 113: 552–557.

Koditschek DE and Rimon E (1990) Robot navigation functions on manifolds with boundary. *Advances in Applied Mathematics* 11(4): 412–442.

Kolmanovsky I, Garone E and Cairano SD (2014) Reference and command governors: A tutorial on their theory and automotive applications. In: *American Control Conference*. pp. 226–241.

Kozlov M, Tarasov S and Khachiyan L (1980) The polynomial solvability of convex quadratic programming. *USSR Comp. Mathematics and Mathematical Physics* 20(5): 223–228.

Kuntz L and Scholtes S (1994) Structural analysis of nonsmooth mappings, inverse functions, and metric projections. *Journal of Math. Analysis and Applications* 188(2): 346–386.

Kwok A and Martnez S (2010) Deployment algorithms for a power-constrained mobile sensor network. *International Journal of Robust and Nonlinear Control* 20(7): 745–763.

LaValle SM (2006) *Planning Algorithms*. Cambridge University Press.

Lionis G, Papageorgiou X and Kyriakopoulos KJ (2007) Locally computable navigation functions for sphere worlds. In: *IEEE International Conference on Robotics and Automation*. pp. 1998–2003.

Liu J (1995) Sensitivity analysis in nonlinear programs and variational inequalities via continuous selections. *SIAM Journal on Control and Optimization* 33(4): 1040–1060.

McMahon J and Snyder V (1898) *Elements of the Differential Calculus*. American Book Company.

Munkres J (2000) *Topology*. 2nd edition. Pearson.

Ó'Dúnlaing C and Yap CK (1985) A retraction method for planning the motion of a disc. *Journal of Algorithms* 6(1): 104 – 111.

Okabe A, Boots B, Sugihara K and Chiu SN (2000) *Spatial Tessellations: Concepts and Applications of Voronoi Diagrams*, volume 501. 2nd edition. John Wiley & Sons.

Pacelli V, Arslan O and Koditschek DE (2018) Integration of local geometry and metric information in sampling-based motion planning. In: *(in press) IEEE International Conference on Robotics and Automation*.

Paranjape AA, Meier KC, Shi X, Chung SJ and Hutchinson S (2015) Motion primitives and 3D path planning for fast flight through a forest. *The International Journal of Robotics Research* 34(3): 357–377.

Paternain S, Koditschek DE and Ribeiro A (2017) Navigation functions for convex potentials in a space with convex obstacles. *IEEE Transactions on Automatic Control* .

Paternain S and Ribeiro A (2016) Stochastic artificial potentials for online safe navigation. *(submitted to) IEEE Transactions on Automatic Control* .

Petersen KB and Pedersen MS (2012) *The Matrix Cookbook*. Technical University of Denmark.

Pierson A and Rus D (2017) Distributed target tracking in cluttered environments with guaranteed collision avoidance. In: *International Symposium on Multi-Robot and Multi-Agent Systems*. pp. 83–89.

Pimenta LC, Kumar V, Mesquita RC and Pereira GA (2008) Sensing and coverage for a network of heterogeneous robots. In: *IEEE Conference on Decision and Control*. pp. 3947–3952.

Rimon E and Koditschek DE (1992) Exact robot navigation using artificial potential functions. *IEEE Transactions on Robotics and Automation* 8(5): 501–518.

Rockafellar R (1985) Lipschitzian properties of multifunctions. *Nonlinear Analysis: Theory, Methods & Applications* 9(8): 867–885.

Shapiro A (1988) Sensitivity analysis of nonlinear programs and differentiability properties of metric projections. *SIAM Journal on Control and Optimization* 26(3): 628–645.

Simmons R (1996) The curvature-velocity method for local obstacle avoidance. In: *IEEE International Conference on Robotics and Automation*. pp. 3375–3382.

Stewart J (2012) *Calculus: Early Transcendentals*. 7th edition. Cengage Learning.

Szeliski R (2011) *Computer Vision: Algorithms and Applications*. Springer.

Trautman P, Ma J, Murray RM and Krause A (2015) Robot navigation in dense human crowds: Statistical models and experimental studies of humanrobot cooperation. *The International Journal of Robotics Research* 34(3): 335–356.

van den Berg JP and Overmars MH (2005) Using workspace information as a guide to non-uniform sampling in probabilistic roadmap planners. *The International Journal of Robotics Research* 24(12): 1055–1071.

Vasilopoulos V, Arslan O, De A and Koditschek DE (2017) Sensor-based legged robot homing using range-only target localization. In: *IEEE International Conference on Robotics and Biomimetics*. pp. 2630–2637.

Vasilopoulos V, Vega-Brown W, Arslan O, Roy N and Koditschek DE (2018) Sensor-based reactive symbolic planning in partially known environments. In: *(in press) IEEE International Conference on Robotics and Automation*.

Wang M, Wang Z, Paudel S and Schwager M (2018) Safe distributed lane change maneuvers for multiple autonomous vehicles using buffered input cells. In: *(in press) IEEE International Conference on Robotics and Automation*.

Webster R (1995) *Convexity*. Oxford University Press.

Wilmarth SA, Amato NM and Stiller PF (1999) MAPRM: a probabilistic roadmap planner with sampling on the medial axis of the free space. In: *IEEE International Conference on Robotics and Automation*, volume 2. pp. 1024–1031.

Wooden D, Malchano M, Blankespoor K, Howardy A, Rizzi AA and Raibert M (2010) Autonomous navigation for BigDog. In: *IEEE International Conference on Robotics and Automation*. pp. 4736–4741.

Wright S and Nocedal J (1999) *Numerical Optimization*. Springer.

Zhou D, Wang Z, Bandyopadhyay S and Schwager M (2017) Fast, on-line collision avoidance for dynamic vehicles using buffered voronoi cells. *IEEE Robotics and Automation Letters* 2(2): 1047–1054.